Greenland Fracture Zone-East Greenland Ridge(s) revisited: Indications of a C22-change in plate motion?

Døssing, Arne; Funck, T.

Published in:
Journal of Geophysical Research: Atmospheres

Link to article, DOI:
10.1029/2011JB008393

Publication date:
2012

Document Version
Publisher's PDF, also known as Version of record

Greenland Fracture Zone–East Greenland Ridge(s) revisited: Indications of a C22-change in plate motion?

A. Døssing[1] and T. Funck[2]

Received 27 March 2011; revised 24 October 2011; accepted 3 November 2011; published 20 January 2012.

[1] Changes in the lithospheric stress field, causing axial rift migration and reorientation of the transform, are generally proposed as an explanation for anomalously old crust and/or major aseismic valleys in oceanic ridge-transform-ridge settings. Similarly, transform migration of the Greenland Fracture Zone and separation of the 200-km-long, fracture-zone-parallel continental East Greenland Ridge from the Eurasia plate is thought to be related to a major change in relative plate motions between Greenland and Eurasia during the earliest Oligocene (Chron 13 time). This study presents a reinterpretation of the Greenland Fracture Zone – East Greenland Ridge based on new and existing geophysical data. Evidence is shown for two overstepping ridge segments (Segments A and B) of which Segment A corresponds to the already known East Greenland Ridge while Segment B was not detected previously. Interpretation of sonobuoy data and revised modeling of existing OBS data across Segment B indicate a continental composition of the segment. This interpretation is supported by magnetic anomaly data. The Segments A and B are bounded by portions of the Greenland Fracture Zone with a distinct ∼10° difference in strike. This is suggested to relate to an early episode of transform migration and reorientation of the lithospheric stress field around Chron 22 time, i.e., shortly after the Eocene breakup in the northern NE Atlantic. These findings contradict with previous interpretations of the fracture zone, which infer simple pre-C13 strike-slip kinematics.

Citation: Døssing, A., and T. Funck (2012), Greenland Fracture Zone–East Greenland Ridge(s) revisited: Indications of a C22-change in plate motion?, *J. Geophys. Res.*, *117*, B01103, doi:10.1029/2011JB008393.

1. Introduction

[2] Passive margins bordering the northern NE Atlantic record the prolonged history of continental breakup between the Laurentian and Eurasian plates since the late Paleozoic [e.g., *Surlyk et al.*, 1981; *McClay et al.*, 1986; *Faleide et al.*, 1993; *Hamann et al.*, 2005; *Faleide et al.*, 2008; *Doré et al.*, 2008]. Following continental break-up in the earliest Eocene (C24B, 53.3 Ma; all age correlations according to *Cande and Kent* [1995]), early Cenozoic sea floor spreading (C24B – C13 (earliest Oligocene)) is generally considered a left-stepping, ridge-transform-ridge system between the Mohns Ridge in the Greenland Basin and an early spreading ridge segment or a region of intense extension in the Boreas Basin (Figure 1). The two "spreading regimes" were linked by the NW-SE trending Greenland Fracture Zone (GFZ), constituting the western border of the De Geer Mega-Shear Region (DGMR) (Figure 1, lower right inset) [*Mosar and Opsal*, 2002; *Mosar et al.*, 2002; *Faleide et al.*, 1993; *Døssing et al.*, 2008]. During the earliest Oligocene (C13), a counter-clockwise rotation in the stress field caused spreading within the DGMR to concentrate along proto-Knipovich Ridge segments. This terminated most transcurrent movements along the GFZ and caused the East Greenland Ridge (EGR) to be rifted off and transferred from the Eurasian plate to the North America – Greenland plate, [e.g., *Mosar et al.*, 2002; *Døssing et al.*, 2008; *Engen et al.*, 2008; *Faleide et al.*, 2008]. Today, this fracture-zone-parallel ridge rises from the seabed about 170 km to the west of the Mohns-Knipovich ridges and runs for 200 km to the north of the GFZ [*Døssing et al.*, 2008].

[3] Plate tectonic models of the DGMR are based almost solely on sporadic outcrops along its borders in North Greenland (Trolle Land Fault Zone) [*Haakansson and Stemmerik*, 1989; *Haakansson and Pedersen*, 2001] and Spitsbergen (Svalbard) [*Harland*, 1969] as well as on numerous seismic studies along the SW Barents Sea – Svalbard sheared margins (Figure 1, lower right inset) [e.g., *Faleide et al.*, 1993, 2008]. In contrast, the lack of borehole control, few high-resolution seismic profiles and poor aeromagnetic data significantly hamper the understanding of the GFZ – EGR, where the acquisition of geophysical data is complicated by sea ice and the remote location. This lack of data poses significant uncertainties in existing plate tectonic models.

[4] Recent interpretations [*Døssing et al.*, 2008] of ocean bottom seismometer (OBS), gravity and multi-channel seismic (MCS) data across the EGR (Line 1 (GEUS2002-1), for

[1]National Space Institute, DTU Space, Copenhagen, Denmark.
[2]Geological Survey of Denmark and Greenland, Copenhagen, Denmark.

0148-0227/12/2011JB008393

location see Figure 2a) showed that the basement ridge is bounded to the southwest by a deep half-graben, located in oceanic crust in the Greenland Basin (Figure 2b, 0–80 km), while a deep sedimentary faulted basin bounds the ridge to the north (Figure 2b, 115–150 km). The faulted boundaries were interpreted as expressions of the GFZ to the southwest and a related fault system to the north (Figure 2a). Seismic modeling along the ridge (Line 2 (GEUS2002-2), for location see Figure 2a) suggested that the EGR constitutes a single continental sliver (6–7-km-thick) overlain by two (meta) sedimentary layers (2-km-thick in total) (Figures 2b and 2c, 100–120 km and 65–150 km, respectively). Interpretation of continental crust has also been inferred from bathymetric data and plate reconstruction models, [e.g., *Engen et al.*, 2008; *Faleide et al.*, 2008]. Immediately to the northwest of the EGR, seismic modeling [*Døssing et al.*, 2008] indicated a

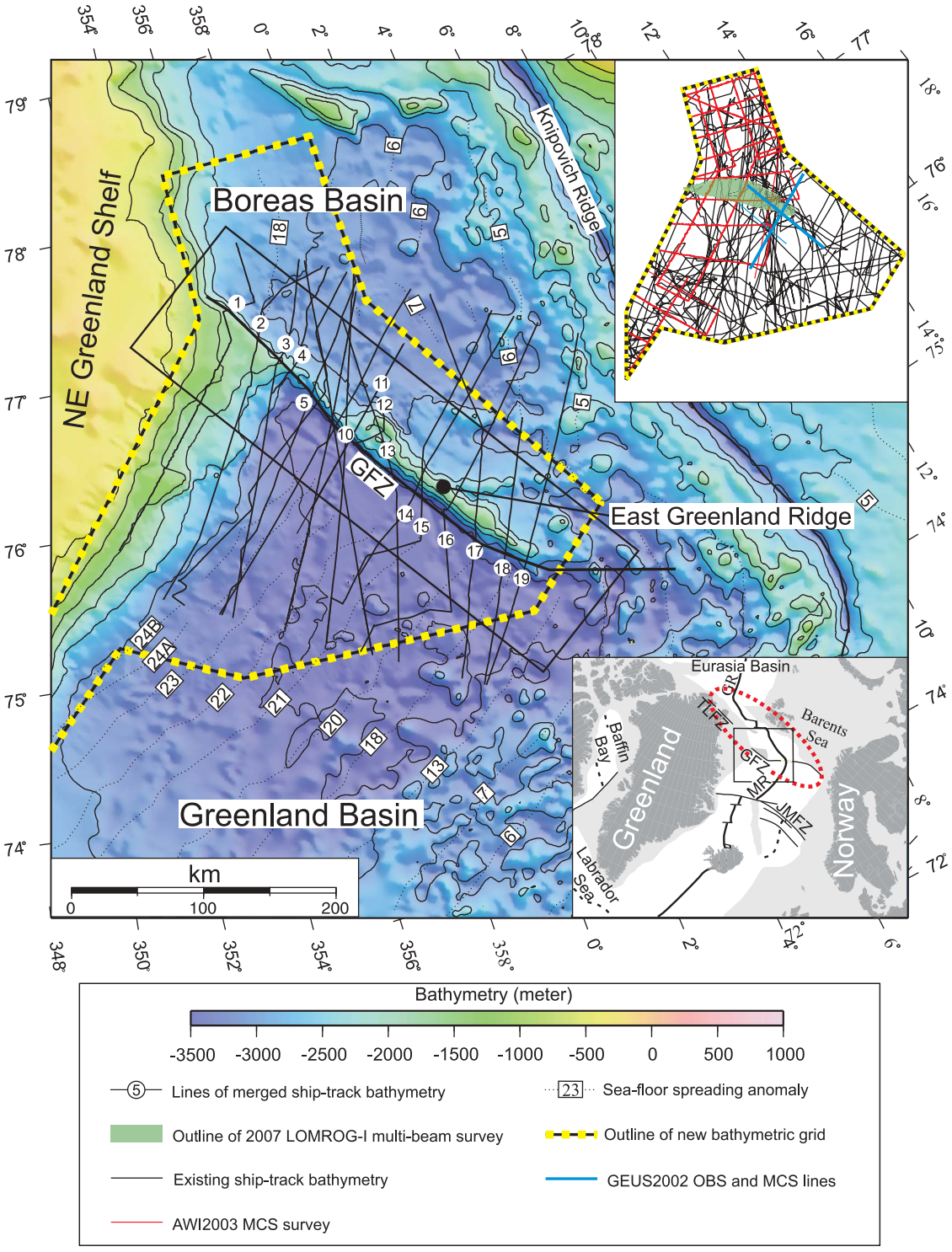

Figure 1

30-km-wide zone (Figure 2c; 40–70 km) of very thin crust (down to ~3 km thick), increased lower crustal velocities (7.2–7.7 km/s) and weak to absent reflections from the Moho, while farther to the northwest (Figure 2c, 0–40 km) the crust was interpreted to thicken gradually beneath the NE Greenland margin. The anomalous crust near km 50 (Figure 2c) was suggested to be the result of extreme pre-C13 (earliest Oligocene) crustal extension in a structural accommodation zone between the EGR and the NE Greenland margin. This interpretation was supported by the *IBCAO Version* 1.0 gridded ship-track bathymetric model of *Jakobsson et al.* [2000], showing a smooth bathymetric low in this area (Figure 2a). However, *IBCAO Version* 1.0 is of limited resolution near the GFZ – EGR and is based on vintage ship and submarine bathymetric surveys of which some are contaminated by positional errors. Furthermore, the northwesternmost 40 km of Line 2 (Figure 2c) was not well-constrained by wide-angle seismic data due to unreversed ray-coverage and noisy data. Hence, the shape of the Moho in this part of the area was poorly constrained and guided by the assumption that the Moho should deepen towards the NE Greenland margin [*Døssing et al.*, 2008]. Moreover, given that this area was not the main focus of their paper, *Døssing et al.* [2008] modeled a simplified intra-sedimentary and top-basement geometry here.

[5] We present a revised interpretation of the GFZ – EGR based on new and existing geophysical data. This includes quality-controlled vintage ship soundings, existing seismic reflection and refraction data, the latest global satellite gravity model [*Andersen et al.*, 2008] as well as new multi-beam data, MCS reflection data, sonobuoy seismic data and ship-track magnetic anomaly data. A new 2.5 × 2.5 km bathymetric grid is compiled for the GFZ – EGR and combined interpretation of the data sets significantly improves the understanding of the region, in particular the early Cenozoic evolution. We present evidence of a hitherto unknown segmentation of the EGR, which we interpret to be the result of a possible earliest Eocene (C22) transform migration and reorientation of the GFZ.

2. Data and Processing

2.1. Seismic Data

[6] In addition to the OBS-MCS Lines 1 and 2, we present interpretations of the single channel seismic Line 3 (V3010) and the MCS Lines 4 (LOMROG2007-4) and 5 (AWI2003-0165) (for location see Figure 2a). The NE-SW trending Line 3 crosses the EGR to the southeast of Line 1 and was acquired by Lamont-Doherty Observatory during the Vema Cruise 30 in 1973. The WNW-ESE trending Line 4 was collected during the 2007 LOMROG-I expedition and extends from the EGR onto the outer NE Greenland Shelf (Figure 3a). The seismic equipment was designed to withstand sea ice, which was encountered at the NW-end of the line. The seismic source was a linear air gun cluster consisting of two GI and one G guns with a total volume of 9.9 L (605 in^3); shot interval was 25 m. A 200-m-long digital streamer with 32 channels (6.25 m group spacing) was towed behind the air gun cluster. Both the array and the streamer had a nominal depth of 20 m. However, within ice-covered areas this depth was variable [*Jakobsson et al.*, 2008a]. The basic processing sequence included bandpass filtering, user defined spectral shaping filtering, spike and noise burst editing, shot gather *f-k* filter and resample to 2 ms, final geometry and amplitude recovery and post-stack constant velocity migrations.

[7] The length of the seismic streamer used for the collection of Line 4 was not sufficient to obtain seismic velocities of the sedimentary layers along the line. For this reason, the acquisition was complemented by recordings from sonobuoys (type AN/SSQ-53D(2) by Ultra Electronics). A total of six buoys (Figures 2a and 3b) were deployed from the ship during the acquisition of the seismic reflection data. The expendable buoys were equipped with a hydrophone (depth of 30 m) and the signals were radioed back to the ship where they were recorded on a Taurus seismometer.

[8] The final SSW–NNE trending Line 5 (Figure 2a) is part of a regional MCS survey acquired by the Alfred Wegener Institute in 2003 with a 600 m streamer and a 6.25 m receiver group interval. Shots were fired every 35–40 m [*Berger and Jokat*, 2008]. Processing procedures and examples of interpretations of some of the AWI lines (but not Line 5) are described by *Berger and Jokat* [2008].

2.2. Marine Magnetic Data

[9] *Døssing et al.* [2008] presented reduced marine gravimetric data acquired along Lines 1 and 2 to support the results of the wide-angle modeling. In addition, we present the marine magnetic data along these lines. The data were reduced by removing the Definitive Geomagnetic Reference Field (DGRF) 2005 model and the diurnal events as recorded by the geomagnetic base station in Ny Ålesund (Svalbard) (http://geo.phys.uit.no/viewasc/).

Figure 1. Bathymetry of the study area. Interpretation of sea-floor spreading magnetic anomalies adapted from *Talwani and Eldholm* [1977] and *Engen et al.* [2008]. Lines 1–19 represent merged lines of ship-track bathymetry presented in Figure 5. Black box outlines area shown in Figures 2a and 4. Upper right inset: Bathymetric information used in new bathymetry grid. Black lines: Quality-screened vintage ship-track data. Red lines: AWI2003 MCS survey [*Berger and Jokat*, 2008, 2009]. Blue lines: GEUS2002 OBS and MCS survey [*Døssing et al.*, 2008]. Lower right inset: Plate tectonic features of the northern NE Atlantic–Arctic Ocean. Dashed red line: Outline of the major DGMR which acted as a Mesozoic–early Cenozoic region of dextral lithospheric stress transfer between the extensional regimes in the northern North Atlantic and the SW Eurasia Basin [*Harland*, 1969; *Haakansson and Pedersen*, 1982; *Eldholm et al.*, 1987; *Faleide et al.*, 1993]. In a pre-drift setting, the sheared western boundaries of DGMR are outlined by the TLFZ in North Greenland and the GFZ [*Faleide et al.*, 1993; *Zinck-Jørgensen*, 1994; *Døssing et al.*, 2008, 2010]. Black box shows the outline of the study area. DGMR, De Geer Mega-Shear Region; GB, Greenland Basin; GFZ, Greenland Fracture Zone; GR, Gakkel Ridge; JMFZ, Jan Mayen Fracture Zone; MR, Mohns Ridge; TLFZ, Trolle Land Fault Zone.

2.3. Bathymetric Data

[10] A multi-beam survey was acquired along Line 4 during the 2007 LOMROG-I survey (for outline see Figure 1, upper right inset). The data were collected using a Kongsberg EM120 multi-beam echo sounder, which was connected to the Global Positioning System (a Thales DG16 GPS receiver) [*Jakobsson et al.*, 2008a]. In addition, we have analyzed all ship and submarine bathymetric soundings in the study area (available from National Geophysical Data Center, NGDC: http://www.ngdc.noaa.gov/mgg/geodas/

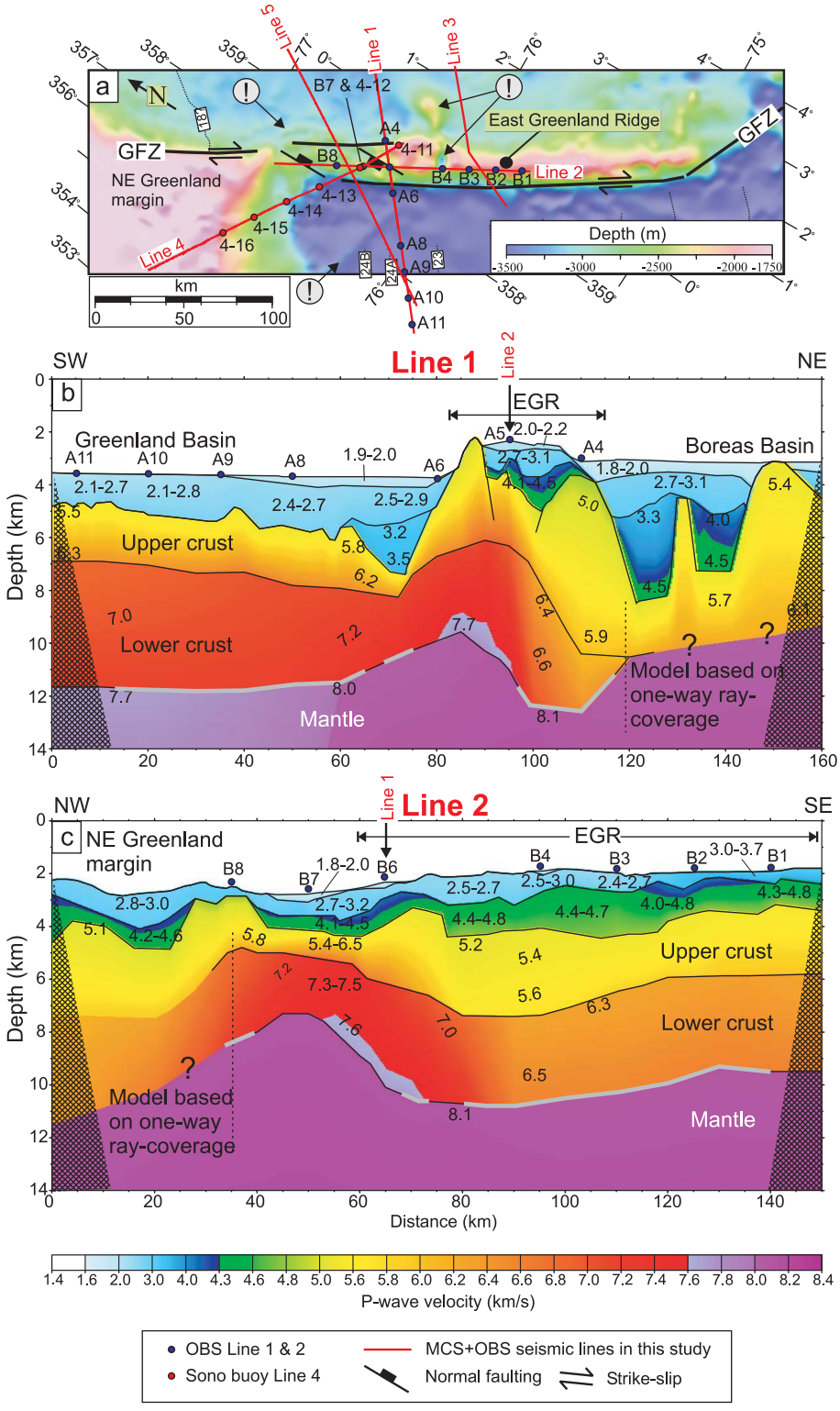

Figure 2

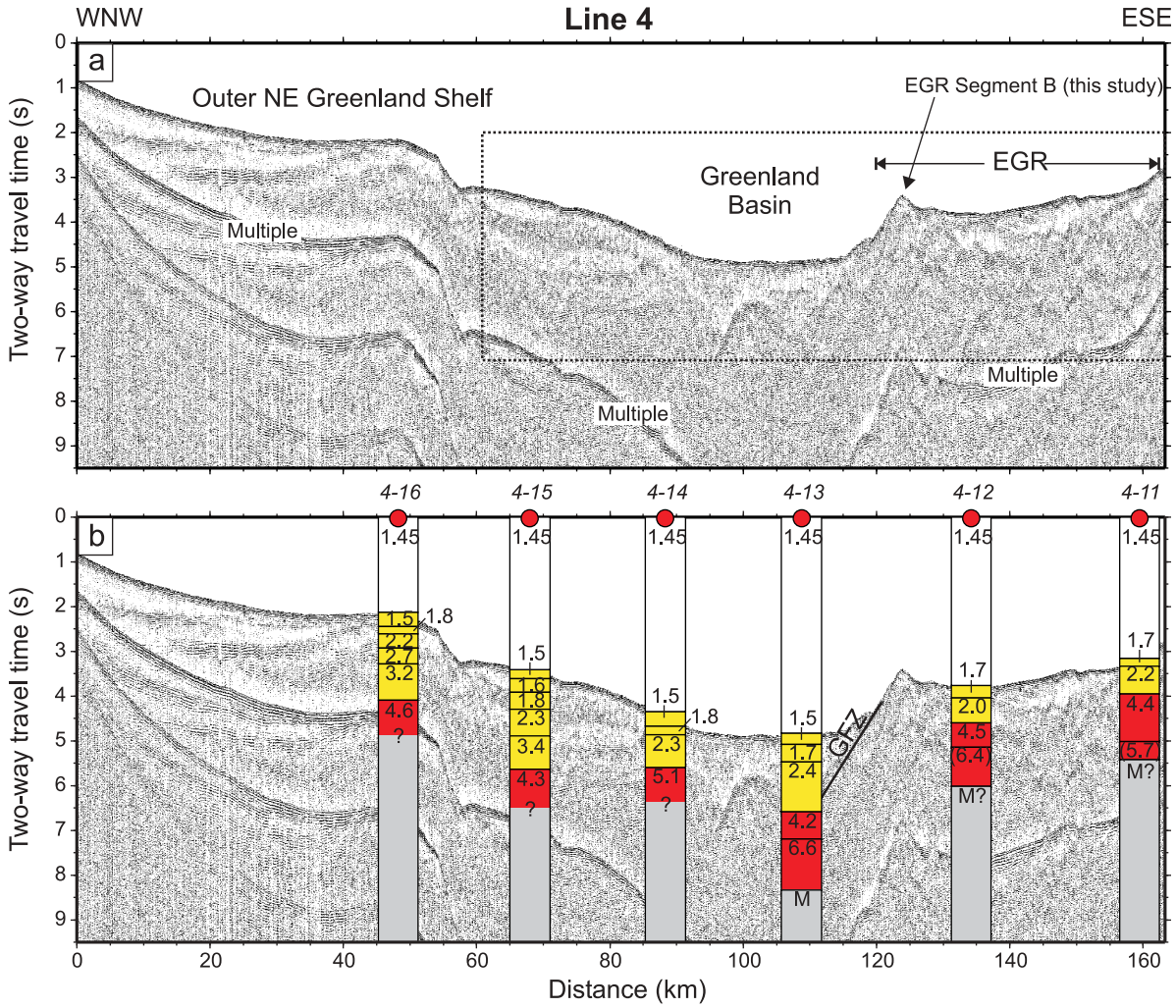

Figure 3. (a) Stacked record section of Line 4 (LOMROG 2007) that extends from the EGR onto the outer NE Greenland Shelf (for location see Figure 2a). The area in the dotted black box is shown with interpretation in Figure 6b (top). (b) Seismic reflection record shown together with the velocity models at the sonobuoy deployment position (red circles; corresponding to a distance of 0 km in Figure 8); velocities are specified in km/s. White areas present the water column; sedimentary layers are drawn in yellow; red colors show basement and crustal rock; the base of the models where the velocities are not determined are marked in grey. The numbers 4–11–4–16 refer to sonobuoys along Line 4 (for location see Figure 2a). EGR, East Greenland Ridge; GFZ, Greenland Fracture Zone.

trackline.html). In total, more than 20 vintage ship and submarine survey lines cross the GFZ – EGR and some of them more than once. The lines, which were mainly acquired in the 1970s, were used as input for the 5 × 5 km gridded *IBCAO* Version 1.0 bathymetric model of *Jakobsson et al.* [2000]. We performed a cross-over error analysis between the vintage lines and bathymetric information extracted from the modern seismic Lines 1, 2, 4 and 5 as well as from the

Figure 2. (a) Previous structural interpretation of the GFZ – EGR [e.g., *Døssing et al.*, 2008], superposed on *IBCAO Version* 1.0 [*Jakobsson et al.*, 2000]. Exlamation marks show bathymetric features caused by positional errors in bathymetric survey lines, mainly old submarine surveys from US Naval Research Lab. Note the interpretation of a structural accommodation zone between the EGR and the NE Greenland margin. Red lines: Seismic lines presented in this study. A4–A6, A8–A11, B1–B4 and B6–B8 refer to OBSs along Line 1 and Line 2 and 4–11–4–16 refer to sonobuoys along Line 4. For outline of area, see black box in Figure 1. (b) Preferred velocity model along Line 1 [*Døssing et al.*, 2008]. (c) Preferred velocity model along Line 2 [*Døssing et al.*, 2008] (for location see Figure 2a). Note that the upper and lower crustal velocities of 5.2–5.6 km/s and 6.3–6.6 km/s beneath the EGR (Figures 2b and 2c, 100–120 km and 65–150 km, respectively) were interpreted by *Døssing et al.* [2008] as evidence of continental crust, while the high-velocity zone, underlying the thin crust in Line 2 (Figure 2c, 40–70 km) was interpreted as dominantly serpentinized mantle peridotite. Note also that the velocity along Line 2 is based on one-way ray-coverage to the NW of OBS B8. Abbreviations are: EGR, East Greenland Ridge; GFZ, Greenland Fracture Zone; MCS, Multi-Channel Seismic; OBS, Ocean Bottom Seismometer. See text for discussion.

Table 1. Bathymetric Data Used in New Grid

Survey (Leg)	Year of Acquisition	Main Institution
LOMROG-I	2007	Geological Survey of Denmark and Greenland
AWI2003[a]	2003	Alfred Wegener Institute
GEUS2002[b]	2002	Geological Survey of Denmark and Greenland
James C. Ross(JCR) (Leg 14)	1996	British Antarctic Survey
OCEAN DRILLING PROGRAM (Leg 162)	1995	Ocean Drilling Program/Texas A and M
OCEAN DRILLING PROGRAM (Leg 151)	1993	Ocean Drilling Program/Texas A and M
Meteor(M) (Leg 26)	1993	Bundesamt Seeschiffahrt Hydrographie
Bartlett (BARTLT90)	1991	U.S. Navy Naval Research Lab
Polar Sea (PLRSEA90)	1990	U.S. Navy Naval Research Lab
Meteor(MTR) (Leg 71)	1985	Deutsches Hydrographisches Institut
Meteor(MTR) (Leg 61)	1982	Deutsches Hydrographisches Institut
Hayes (B75H02)	1975	U.S. Navy Naval Research Lab
Hayes (74-16-04)	1974	U.S. Navy Naval Research Lab
Hayes (73-16-02)	1973	U.S. Navy Naval Research Lab
Vema 30(Leg 10)	1973	Lamont-Doherty Geological Observatory
Hayes (72-16-06)	1972	U.S. Navy Naval Research Lab
Hayes (72-11-05)	1972	U.S. Navy Naval Research Lab
Vema 29(Leg 10)	1972	Lamont-Doherty Geological Observatory
Lynch(LY) (Legs C & D)	1972	U.S. Navy
Hayes (71-11-04)	1971	U.S. Navy Naval Research Lab
Vema 28(Legs 2 and 3)	1970	Lamont-Doherty Geological Observatory
Vema 27(Legs 3 and 4)	1969	Lamont-Doherty Geological Observatory
Vema 23(Leg 4)	1966	Lamont-Doherty Geological Observatory

[a]Entire seismic survey used of which interpretation of selected lines were recently published [*Berger and Jokat*, 2008, 2009].
[b]Entire survey (three lines) used of which Lines 1 and 2 were published by *Døssing et al.* [2008].

AWI2003 MCS survey (for location see Figure 1). The outcome showed that several of the old survey lines, in particular lines obtained from submarines, are contaminated by large positional errors, which creates peculiar bathymetric features (some of them marked in Figure 2a). We, therefore, compiled a new 2.5 × 2.5 km bathymetric subgrid in the GFZ – EGR area (for outline see Figure 1) based on quality-controlled vintage soundings and Lines 1, 2, 4 and 5 and the AWI2003 survey (Table 1 and Figure 1, upper right inset). The subgrid was subsequently merged with *IBCAO Version* 2.23 [*Jakobsson et al.*, 2008b] outside the area using the *Geosoft Oasis Montaj* gridnitting procedure.

3. Morpho-structural Analysis

3.1. Bathymetric Interpretation

[11] Interpretation of the new bathymetric (Figure 4) information shows that the GFZ in its southeastern section is flanked by a structurally distinct, NW–SE oriented ridge segment (here termed *EGR Segment A*), which is approximately 180-km-long and 20-km-wide at its base (Figures 4a and 4b). The water depth within Segment A is generally less than 2000 m and shoals to ~1700 m. At the northwestern termination of Segment A and partly overlapping its southwest edge, the fracture zone is flanked by another ridge segment (here termed *EGR Segment B*), which is approximately 100-km-long, 5-km-wide and defined by water depths of more than 2500 m (Figures 4a, 4b, and 4c). Hence, the ridge segments form an *en echelon*, right-stepping ridge pattern where Segment A appears to have moved to the north of Segment B along a portion of the GFZ located between the segments. Note that Segment B has a distinct NNW–SSE orientation, implying that a 10–15° angle exists between the two portions of the GFZ that bound Segments A and B (Figure 4a). Comparison of the previous (Figure 2a) and new interpretations (Figure 4a) of the EGR shows that EGR Segment A corresponds to the EGR previously interpreted, while EGR Segment B was not previously detected. Note that the existence and geometry of Segments A and B is also observed in gravity (Figure 4d). The above morpho-structural interpretation along the GFZ – EGR is well-displayed by a compilation of 19 ship-track bathymetric profiles that cross the fracture zone (Figure 5; Lines 1–19, Figure 1). While EGR Segment B (profiles 5–10) is defined by a sharp and narrow ridge crest, EGR Segment A (profiles 14–19) is far more prominent with a broad ridge crest. A 30-km-wide, double ridge crest geometry characterizes the region, where the two segments overlap (here termed the *EGR Central Segment*: profiles 11–13).

[12] To the northwest of EGR Segment B, the shallow outer NE Greenland Shelf terminates to the north towards the deep Boreas Basin along a sharp, 3-km-high and NW–SE trending shelf edge (Figures 4a and 5). We interpret this linear feature as a sheared margin segment (here termed the *NE Greenland Shear Margin*) formed along a northwest continuation of the GFZ.

3.2. Seismic Reflection Interpretation

[13] Interpretation of the MCS Line 5 (Figure 6a, top) shows that EGR Segment B is characterized by a well-defined basement ridge structure with basement rising from

Figure 4. (a) New structural-tectonic interpretation of the GFZ–EGR. Note the interpretation of EGR Segments A and B. The 30-km-long region, where the two segments overlap, is here termed the *EGR Central Segment*. Interpretation of the deep faulted basin from the NW-termination of Segment A, along the NE-flank of Segment B and further along the NE Greenland Shear Margin is based on *Døssing et al.* [2008] and *Berger and Jokat* [2009]. Magnetic lineations are adopted from *Engen et al.* [2008]. See Figure 2a for OBS and sonobuoy station numbers. (b) New 2 × 2 km bathymetric grid based on quality-screened vintage soundings and the GEUS2002 and AWI2003 seismic surveys (see Table 1). Note the distinct ridge crest of the previously undetected EGR Segment B in these data. (c) LOMROG-I 2007 multi-beam bathymetry. (d) Computed 2nd vertical derivative of the Free-air gravity anomaly [*Andersen et al.*, 2008]. Note that EGR Segments A and B are structurally distinct from both gravity and bathymetry. EGR, East Greenland Ridge; GFZ, Greenland Fracture Zone; MCS, Multi-Channel Seismic; OBS, Ocean Bottom Seismometer.

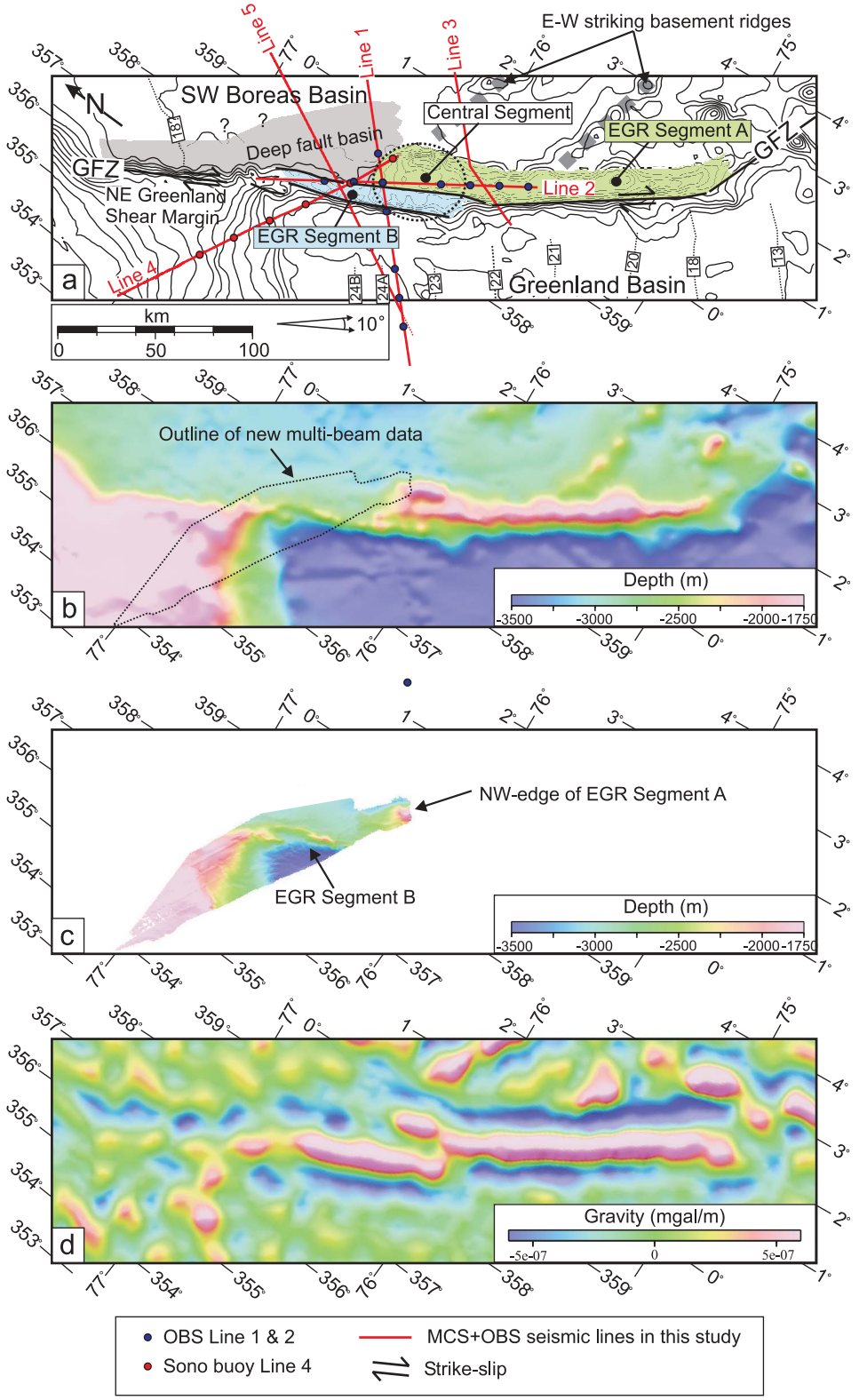
E-W striking basement ridges
Line 5
Line 1
Line 3
SW Boreas Basin
Central Segment
EGR Segment A
GFZ
Deep fault basin
NE Greenland
Shear Margin
Line 2
EGR Segment B
Line 4
Greenland Basin
a
km
0
50
100
10°
Outline of new multi-beam data
b
Depth (m)
-3500
-3000
-2500
-2000
-1750
NW-edge of EGR Segment A
EGR Segment B
c
Gravity (mgal/m)
-5e-07
0
5e-07
d
OBS Line 1 & 2
Sono buoy Line 4
MCS+OBS seismic lines in this study
Strike-slip

Figure 4

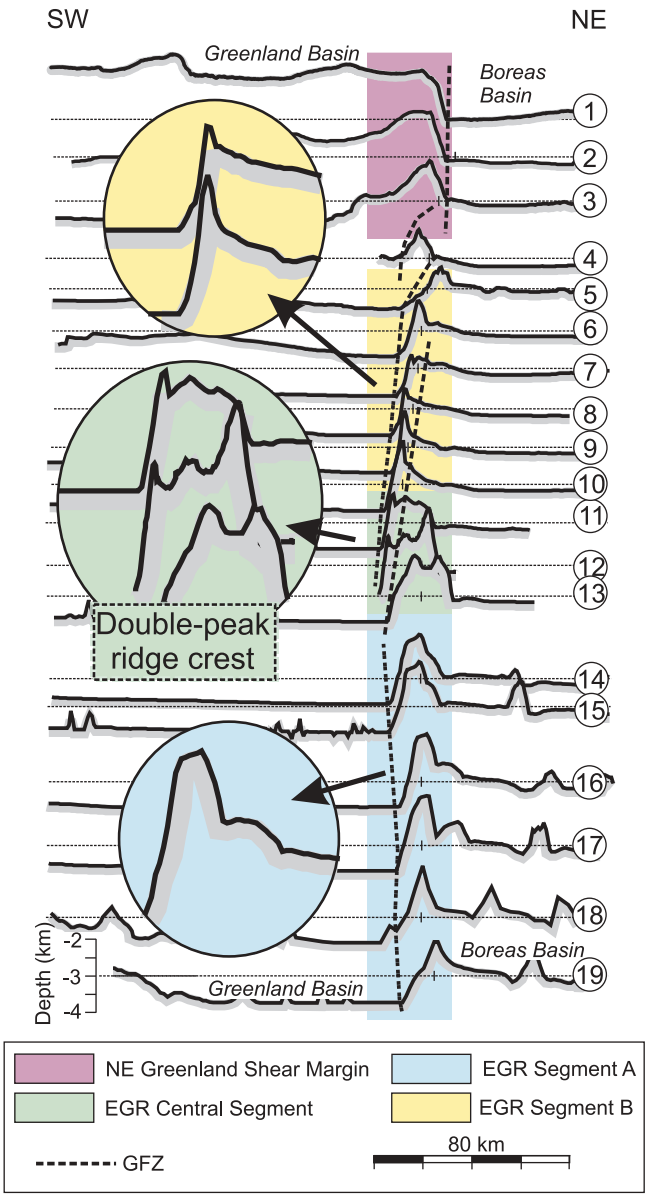

Figure 5. Compilation of 19 ship-track bathymetric profiles across the GFZ (for location of the profiles see Figure 1). The profiles represent merged ship-track lines that have been projected onto lines normal to the GFZ. The sharp ridge crests in profile 18 is due to low sampling density. Note the abrupt shift in seabed asymmetry near profile 4. Thus, profiles 1–3 across the GFZ–NE Greenland Shear Margin show a steep, 1–1.5-km-high NE-facing slope towards the Boreas Basin and a gently dipping SW-flank towards the Greenland Basin, while profiles 5–19 across the GFZ–EGR show a reversed geometry with the SW-facing flank of EGR that rises abruptly 1.5–2.5 km above the seabed in the Greenland Basin and the NE-facing flank that dips relative gently towards the Boreas Basin. We therefore interpret the main portion of the GFZ to be located near profile 4, separating the NE Greenland Shear Margin from EGR Segment B. EGR, East Greenland Ridge; GFZ, Greenland Fracture Zone.

7.6 to 3.4 s two-way travel time (TWT) from the Greenland Basin to the Segment B ridge crest over a distance of ~15 km at the GFZ. Basement then deepens by step-wise faulting to 7.0–7.2 s TWT beneath the southern Boreas Basin, resulting in a total sedimentary thickness of more than 3.3 s TWT. The presence of a fault basin in this area was initially deduced from gravity data [*Døssing et al.*, 2008] and its interpreted northwestward continuation along the NE Greenland Shear Margin (Figure 4a) is supported by recent seismic reflection interpretations [*Berger and Jokat*, 2009].

[14] Interpretation of Line 1 across the EGR Central Segment (Figure 6a, bottom) shows that basement here rises from 7.8 to 3.0 s TWT from the Greenland Basin to the ridge crest over a distance of 12 km. To the north of the EGR, basement deepens to 7.4 s TWT into a deep and narrow fault basin that connects to the northwest with the fault basin along EGR Segment B (Figure 4a) [cf. *Døssing et al.*, 2008]. Line 1 shows that the EGR Central Segment is defined by a complex and broad basement structure, thus reflecting the two overlapping Segments A and B (Figure 6a, bottom). However, while Segment B is well-defined in Line 1 (Figure 6a (bottom), 80–90 km), the record shows only the northwesternmost edge of Segment A (Figure 6a (bottom), 105–120). Here, the sediment-covered basement lies some 1.1 s TWT deeper than basement beneath Segment B and a fault zone of heavily disturbed basement occurs between the two segments. The same fault zone is also interpreted in Line 4 (Figure 6b, top) which also crosses both segments (see Figure 4a). Hence, Lines 1 and 4 support the interpretation that a portion of the GFZ separates Segments A and B. Further to the southeast, Line 3 displays the single, prominent basement ridge of EGR Segment A (Figure 6b, bottom). Similar to Segment B and the Central Segment, Segment A is also flanked by a fault basin to the north. However, seismic (Figure 6b, bottom) and gravity [*Døssing et al.*, 2008] interpretations suggest a less deep (only 500 ms TWT) fault basin here.

[15] *Døssing et al.* [2008] originally proposed that the crustal discontinuity (the GFZ) between EGR and the NE Greenland margin is outlined by the narrow, crustal depression and elevated Moho topography near km 50 in Line 2 (Figure 2c). Here, coincident MCS data also shows evidence of highly faulted basement (Figure 7, 40–60 km). However, the results presented in this study (Figure 4a) shows that the anomalous crust is rather an expression of a portion of the GFZ between EGR Segments A and B. Thus, Line 2 MCS data displays similar faulted and depressed crust farther to the northwest between EGR Segment B and the NE Greenland Shear Margin (Figure 7, 10–25 km), imaging the other portion of the fracture zone. The narrow basement high (Figure 7, 30 km) that separates the two faulted basement regions is interpreted to represent an oblique view of EGR Segment B since the NNW–SSE orientation of this segment is oblique to Line 2 (see Figure 4a).

4. Seismic Velocities and Crustal Structure of EGR Segments A and B

4.1. Results of the Sonobuoy Experiment Along Line 4

[16] Shot positions were determined using the Global Positioning System (GPS). Shots within the radio range of the sonobuoys (ca. 20 km) were extracted from the seismometer, converted to SEGY format and gathered in one

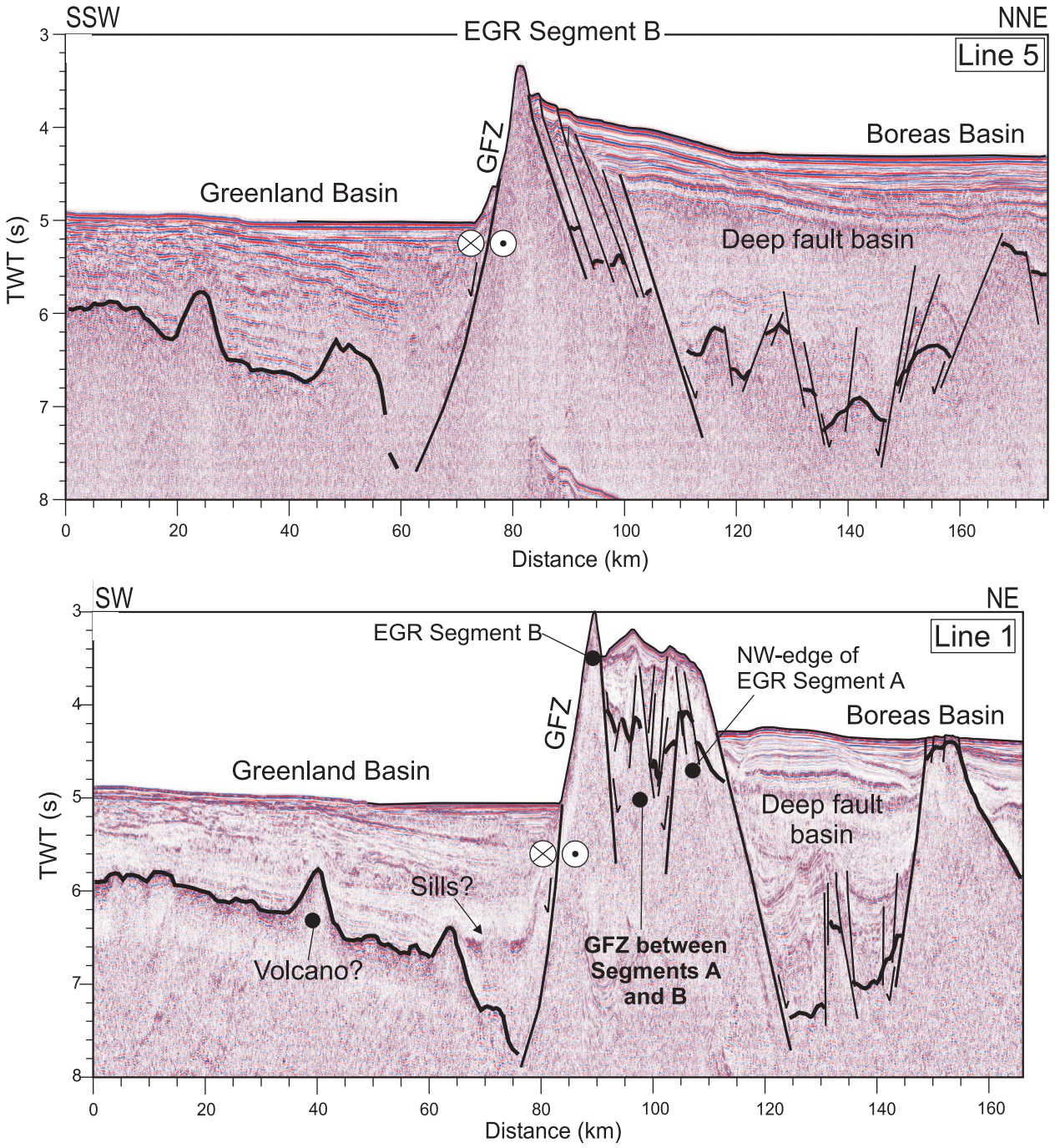

Figure 6a. Interpretation of seismic reflection lines across the GFZ - EGR (for location see Figure 4a). (top) Line 5 (AWI2003-0165) across EGR Segment B. (bottom) Line 1 (GEUS2002-1) across the EGR Central Segment showing both Segment A and B. Note the interpreted volcanic mound and intra-sedimentary sills in the Greenland Basin on Line 1. EGR, East Greenland Ridge; GFZ, Greenland Fracture Zone; TWT, two-way travel time.

file for each buoy. The sonobuoys were freely drifting in the water but not equipped with a navigation system. Hence, the most important processing step was the calculation of the correct shot-receiver distances (offset). This was done by measuring the arrival time of the direct water wave for each shot from which the offset could be calculated using the water sound velocity (1445 m/s) obtained from a CTD (conductivity, temperature, depth) measurement close to the NW-end of Line 4 [*Anderson et al.*, 2007]. Further processing included a deconvolution and a bandpass filter. Subsequently, arrival times of reflected and refracted waves were digitized from the six sonobuoy record sections (4–11 to 4–16) along Line 4 in preparation for velocity modeling (ray tracing) employing the program RAYINVR [*Zelt and Smith*, 1992; *Zelt and Forsyth*, 1994]. For each buoy a two-dimensional velocity model was developed from top to

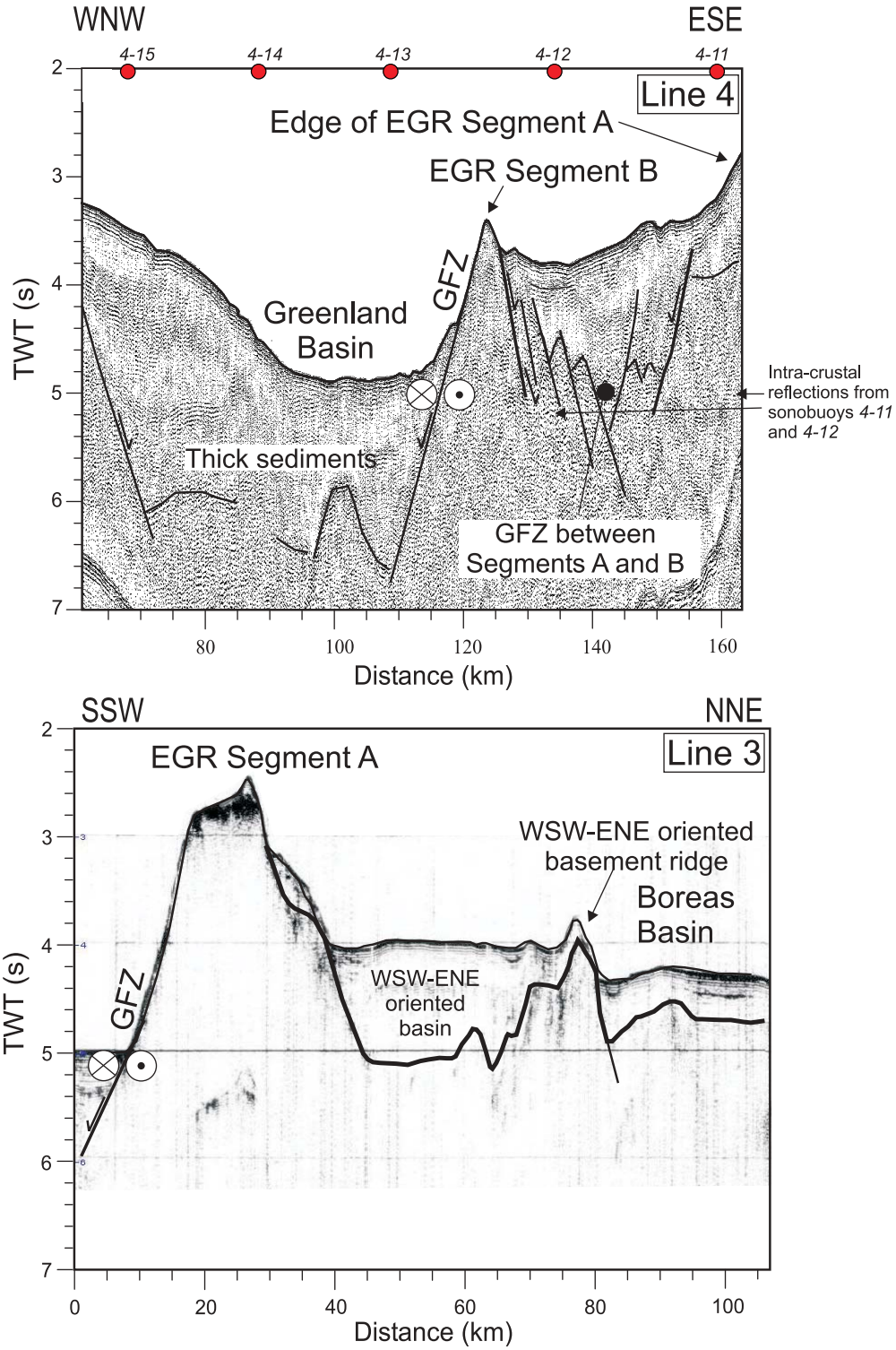

Figure 6b. (top) Line 4 (LOMROG-4) across the EGR Central Segment showing both Segment B and the NW-edge of Segment A. Note the distinct faults that outline the edges of shallow basement over Segments A and B, while the intervening fault zone (GFZ) is characterized by deep, faulted basement that is covered by up to 2.0 s of sediments. (bottom) Line 3 (V3010) across EGR Segment A. EGR, East Greenland Ridge; GFZ, Greenland Fracture Zone; TWT, two-way travel time.

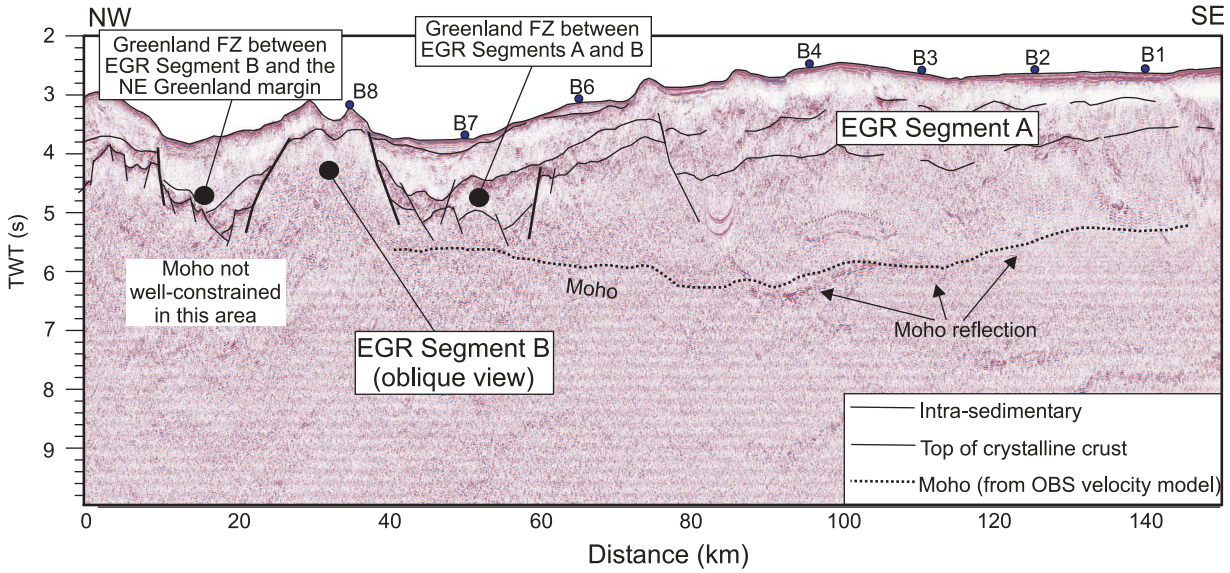

Figure 7. Interpretation of seismic reflection Line 2 (GEUS2002-2), parallel to and along the crest of EGR Segment A and subparallel to EGR Segment B (for location see Figure 4a). Interpretations are modified from *Døssing et al.* [2008]. EGR, East Greenland Ridge; OBS, Ocean Bottom Seismometer; TWT, two-way travel time.

bottom (Figure 8). Normally, the velocities of such unreversed profiles would not be very reliable unless the dip of the subsurface layers is known. This information was provided by the coincident reflection seismic data (Figure 3a). Here the layer boundaries generally correlate with prominent reflectors or a change of the reflectivity pattern. These boundaries were digitized and converted from two-way travel time to depth using the velocities from the velocity model. No lateral velocity variations were used within model layers. Following this forward modeling approach, velocities within individual layers were readjusted by the inverse algorithm in RAYINVR. Upon changes in the velocity model, layer boundaries were adjusted to preserve the fit with the two-way travel times in the reflection seismic data.

[17] Normally, marine refraction seismic experiments are arranged in a common receiver geometry, i.e., a single stationary receiver recording a number of shots. For a drifting sonobuoy, this geometry is no longer valid as the receiver is not stationary [*Bruguier and Minshull*, 1997]. *Bruguier and Minshull* [1997] suggest that the most satisfactory approach for modeling the true geometry of the experiment is to ensure that each shot is located at the correct position and allow the sonobuoy position to move such that the ranges remain correct. However, in reality the direction of drift is unlikely to lie exactly along the direction of the shot line and there will probably be a component of drift out of the plane of the experiment. Therefore the water depth below the sonobuoy may still be incorrect [*Bruguier and Minshull*, 1997]. Due to the unknown component of sonobuoy drift out of the shot line, the position of the buoy was kept stationary at 0 km. When the layer geometry was transferred from the reflection seismic data to the velocity model, the shot positions are displayed at a horizontal distance in the model that corresponds to the corrected offset between the shot and sonobuoy. That way the rays have the correct entry points at the seafloor and at the subsurface layers at the shot position.

[18] Comparison of observed and computed travel times and the preferred two-dimensional velocity models for all sonobuoys on Line 4 are shown in Figure 8. A summary of the model misfit is given in Table 2. The corresponding one-dimensional velocity models show a reasonable correlation between individual sonobuoys (Figure 3b). The top of the sedimentary sequence is characterized by velocities between 1.5 and 2.0 km/s, divided into one to three layers. Thin layers (ca. 200 m) with velocities just above 1.5 km/s were found for buoys 4–13 through 4–16 and indicate a high-water content in the uppermost layer. Underneath the <2.0 km/s sedimentary units, a layer with velocities in the range from 2.0 to 2.6 km/s was identified, with slight variations from station to station. The thickness of this layer varies between 350 m (buoy 4–16) and 1400 m (buoy 4–13). Additional sedimentary layers are present beneath the outer NE Greenland Shelf at the western end of Line 4, where a 1.3-km-thick layer with velocities of 3.4 km/s was observed at buoy 4–15. At the neighboring station 4–16, similar velocities are found (3.2 km/s) below a 0.5-km-thick layer with velocities of 2.7 km/s – a velocity not observed elsewhere on Line 4.

[19] At greater depths, velocities increase to values between 4.2 km/s (buoy 4–13) and 5.1 km/s (buoy 4–14) (Figure 3b). These velocities are interpreted differently along the line. At sonobuoy 4–14, the reflection seismic record shows some stratification within the 5.1 to 5.3 km/s layer, which could suggest a composition of sedimentary rocks. However, this stratification could also be caused by the reverberative gun signature. Given the absence of other sedimentary layers with a velocity of >5.0 km/s along the line, we interpret these high velocities as basement, possibly consisting of metasediments similar to the more than 2-km-thick platform-sequence of Paleoproterozoic sandstones that overlie the Precambrian shield in NE Greenland [cf. *Kalsbeek and Jepsen*, 1983]. In contrast, sonobuoys 4–12 and 4–13 show a variable relief at the top of the 4.2 to

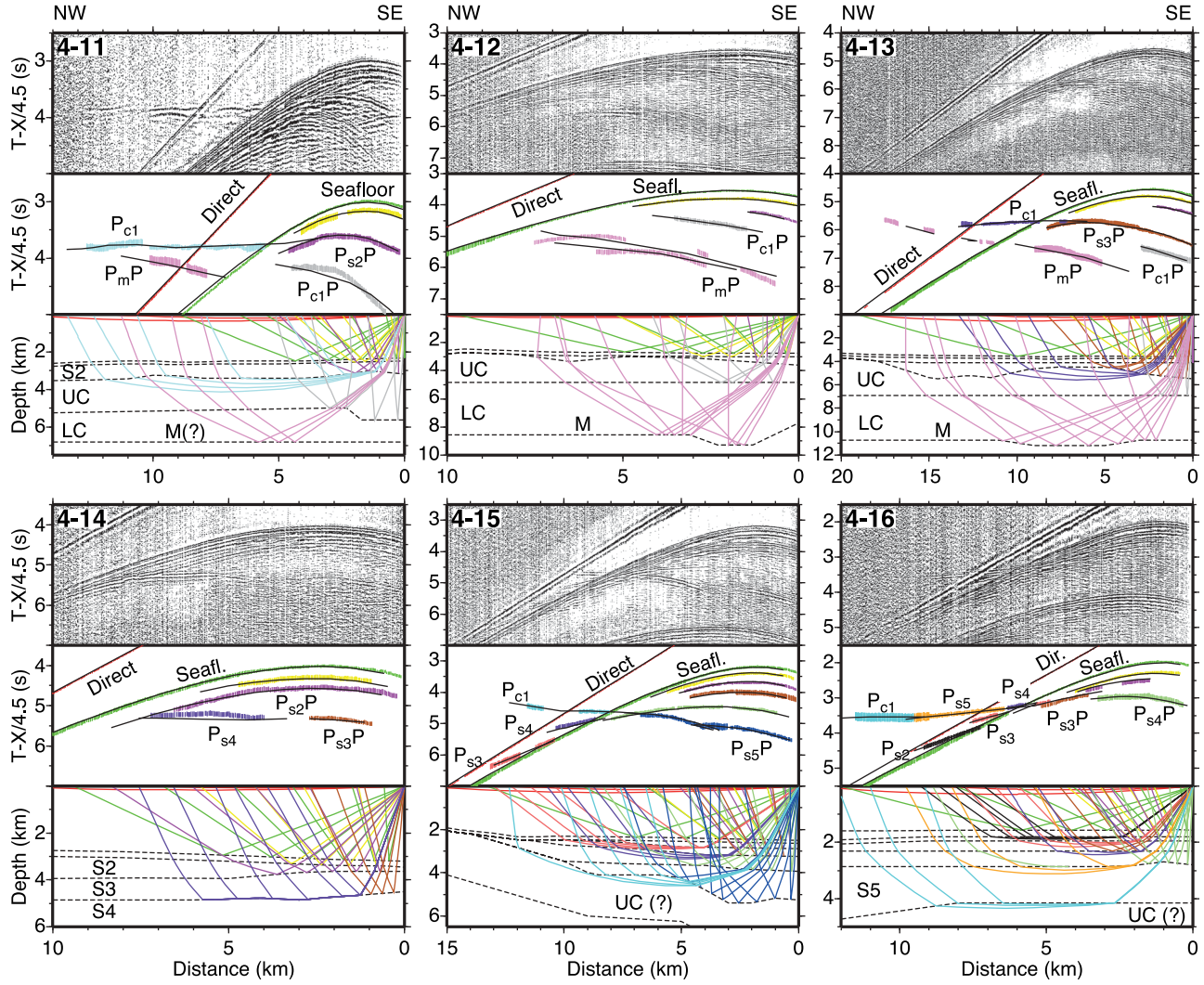

Figure 8. Comparison of observed and calculated travel times (center part of each panel) for sonobuoys 4–11 through 4–16 on Line 4 (for location see Figure 4a), shown together with (bottom) the corresponding ray paths and (top) the record sections. Observed data are indicated by colored bars, with heights representing pick uncertainty; calculated data are indicated by solid lines. Horizontal scale is the model position with the sonobuoy at 0 km; a reduction velocity of 4.5 km/s has been applied for the travel times. Processing includes a deconvolution and a bandpass filter (5–24 Hz). Phase names are $Ps_{(1-5)}$ refractions within sedimentary layers 1 through 5; $Ps_{(1-5)}P$, reflection from the base of sedimentary layers 1 through 5; P_{c1}, refraction in the upper crust/basement; $P_{c1}P$, intra-crustal reflection; P_mP, Moho reflection. Dir., direct wave; LC, lower crust; M, Moho; UC, upper crust; S, sediment layer; Sea., seafloor reflection. Numbers in bottom panel indicate the velocities within individual layers (in km/s). Note that buoy 4–12 mainly samples the crustal velocities and Moho depth beneath EGR Segment B, considering the geometry of the Line 4 sonobuoy experiment with a sailing direction to the WSW and that buoy 4–12 is located a few km to the ENE of the crest of Segment B (see Figure 3b).

5.0 km/s layer, underlain by another layer with velocities of 6.4–6.6 km/s and 6.6–7.0, respectively km/s. Here, the upper layer is interpreted as basement. For the remaining three sonobuoys on the line, the character of the layer with velocities of ~4.5 km/s is not determined (sedimentary rock or crust).

[20] The sonobuoy experiment was designed to obtain good control on the sedimentary velocities. With the known geometry of the sedimentary layers from the coincident reflection seismic data and offsets of generally 4 to 6 km for the sediment reflections ($P_{s1}P$, $P_{s2}P$, $P_{s3}P$) on the sonobuoy

Table 2. Number of Observations (n) RMS Misfit Between Calculated and Picked Travel Times (t_{rms} (ms)) and Normalized X^2 for Individual Sonobuoys on Line 4

Sonobuoy	n	t_{rms} (ms)	X^2
4–11	1487	0.089	8.715
4–12	1071	0.062	1.239
4–13	1831	0.038	1.135
4–14	1210	0.048	0.849
4–15	1785	0.036	0.731
4–16	1186	0.032	0.532

data (Figure 8), sediment velocities are considered to be well constrained (±0.1 km/s). This is in particular the case when additional control was provided by refractions (e.g., buoys 4–14 through 4–16, Figure 8). Below basement, the resolution of upper crustal velocities depends on the existence of constraints from a refraction (P_{c1}) or just from a mid-crustal reflection ($P_{c1}P$). In case of observed refractions, basement velocities are estimated to have an error of 0.2 km/s for buoys 4–11, 4–13, and 4–16 and slightly higher for buoy 4–15 where the basement has more relief. Note that sonobuoy 4–11 samples the northwestern edge of EGR Segment A (for location see Figure 4a). Hence, the crustal velocities of 5.70 km/s (Figure 3b) corresponds well to the wide-angle seismic results of *Døssing et al.* [2008], showing upper and lower crustal velocities of 5.2–5.6 km/s and 6.3–6.6 km/s, respectively, over this segment (Figures 2b and 2c, 100–120 km and 60–150 km, respectively). This supports the interpretation that Segment A is a continental sliver [*Døssing et al.*, 2008].

[21] Crustal velocities based solely on reflections have a high uncertainty since there is no control on the layer geometry from the reflection seismic data. For example, for sonobuoy 4–12 (Figures 3b and 8), upper and lower crustal velocities beneath EGR Segment B can be modeled with 4.5–4.7 km/s and 6.4–6.6 km/s while Moho appears to be located around 8 km depth. However, by varying the Moho topography, an almost equal fit to the observed data can be obtained with lower crustal velocities up to 7.2 km/s. Taking into consideration the relatively large uncertainties in the buoy 4–12 modeling, the results suggest that Segment B is characterized by somewhat lower crustal velocities than suggested for the same area by *Døssing et al.* [2008] (see Figure 2c, 35 km).

4.2. Revised OBS Wide-Angle Modeling Along Line 2

[22] The northwestern most 40 km of the original Line 2 velocity model (Figure 2c) was based on the unreversed observations on OBSs B7 and B8. In addition, OBS B8 was severely affected by noise. The model was therefore guided by the assumption that the crust should thicken beneath the NE Greenland margin [*Døssing et al.*, 2008]. We produced a revised wide-angle model of the data from OBSs B7 and B8, following the modeling procedure described by *Døssing et al.* [2008]. The re-modeling was guided by the new morpho-structural interpretation (Figure 4a) and the crustal seismic velocities obtained from the sonobuoy station 4–12 (Figure 3b), which mainly samples the velocities beneath EGR Segment B. These velocities were therefore used to constrain crustal velocities from the noisy OBS B8, which is located directly over Segment B, while OBS B7 is located in the GFZ between Segments A and B (see Figures 4a and 7).

[23] Plotted seismic recordings from OBS B7 (Figure 9) and OBS B8 (Figure 10) reveal markedly different geometries, reflecting the different crustal geometries within the GFZ and beneath Segment B. On OBS B7 (Figure 9), a lower crustal phase (P_{c2}) with a velocity of >7.0 km/s becomes a first arrival at offsets of 7 km. In contrast, OBS B8 displays an upper crustal phase (P_{c1}) with a velocity of ~5.5 km/s that can be identified up to offsets of 18 km to the northwest and up to 10–15 km to the southeast (Figure 10). A weak lower crustal phase (P_{c2}) with velocities of 6.3–6.7 km/s is observed at offsets between ~15 and 20 km. The P_n phase is recognizable for offsets larger than 15 km but becomes rather weak for offsets larger than 25–30 km. No clear reflection is observed from the Moho (P_mP) on OBS B8, which is possibly due to the low signal-to-noise ratio (Figure 10). OBS B7 displays a weak P_mP phase (Figure 9).

[24] The revised velocity model along Line 2 introduces a two-layered, 6-km-thick crystalline crust beneath EGR Segment B (Figure 11b, 20–40 km) with upper and lower crustal velocities of 4.7–5.9 km/s and 6.3–6.7 km/s and another zone of very thin crust at the GFZ between EGR Segment B and the NE Greenland margin (Figure 11b, 15–20 km). The seismic sections for OBSs B7 and B8 show that the computed travel times fit the observed arrivals well (Figures 9 and 10), supporting the interpretation that Segment B is bounded by portions of the GFZ on either side. A summary of the new and original model misfit for important phases is given in Table 3. The new values are directly comparable to or even better (P_n-phase in particular) than the previous values of *Døssing et al.* [2008]. However, the unreversed ray-coverage to the northwest of OBS B8 implies that alternative models may exist to the model of *Døssing et al.* [2008] and the revised model presented in this study.

5. Discussion

5.1. Crustal Affinity of EGR Segment B

[25] Neither the sonobuoy modeling of station 4–12 along Line 4 (section 4.1) nor the revised OBS modeling along Line 2 (section 4.2) provide unequivocal constraints on the EGR Segment B crustal affinity given the uncertainties in the data quality. However, the crustal velocities around OBS B8 generally resemble those from OBSs B1–B4 located on the continental Segment A (Figure 11b), while the lower crustal velocities around B8 are a little low for oceanic layer 3 as modeled in the Greenland Basin crust (Figure 11a, 0–60 km). Also, the upper crust beneath OBS B8 with a thickness of 3–4 km is too thick for oceanic layer 2 which is close to 2 km on average [*White et al.*, 1992]. We tested the new velocity model for Line 2 by two-dimensional gravity modeling. With the original velocity model, *Døssing et al.* [2008] noted that the initial gravity field (obtained directly by converting velocities to densities using the empirical mean velocity-density conversion values of *Ludwig et al.* [1970]) and the observed field differed by tens of mgal in several places, e.g. a −30 mgal misfit at the northwesternmost 30 km of the line (Figure 11b). This misfit was reduced by increasing the lower crustal density by ~100 kg/m^3 to >2900 kg/m^3. With this and other minor corrections along the line, a final density model was obtained and characterized by deviations of maximum ±5 mgal and an RMS misfit of 3–4 mgal [*Døssing et al.*, 2008]. We obtain an improved initial and similar final fit (Figure 11b) by using upper and lower crustal densities of 2580–2750 kg/m^3 beneath EGR Segment B and 2670–2850 kg/m^3 beneath the NE Greenland margin. These densities are comparable to Segment A continental crustal densities [e.g., *Døssing et al.*, 2008].

[26] Based on the seismic results (section 4) and the above discussion, we tentatively suggest a possible continental affinity of the crust on Segment B. This interpretation is further supported by ship-track magnetic anomaly data along Line 2 (Figure 11b), which shows only weakly undulating anomalies along the line with an overall trend that tends to

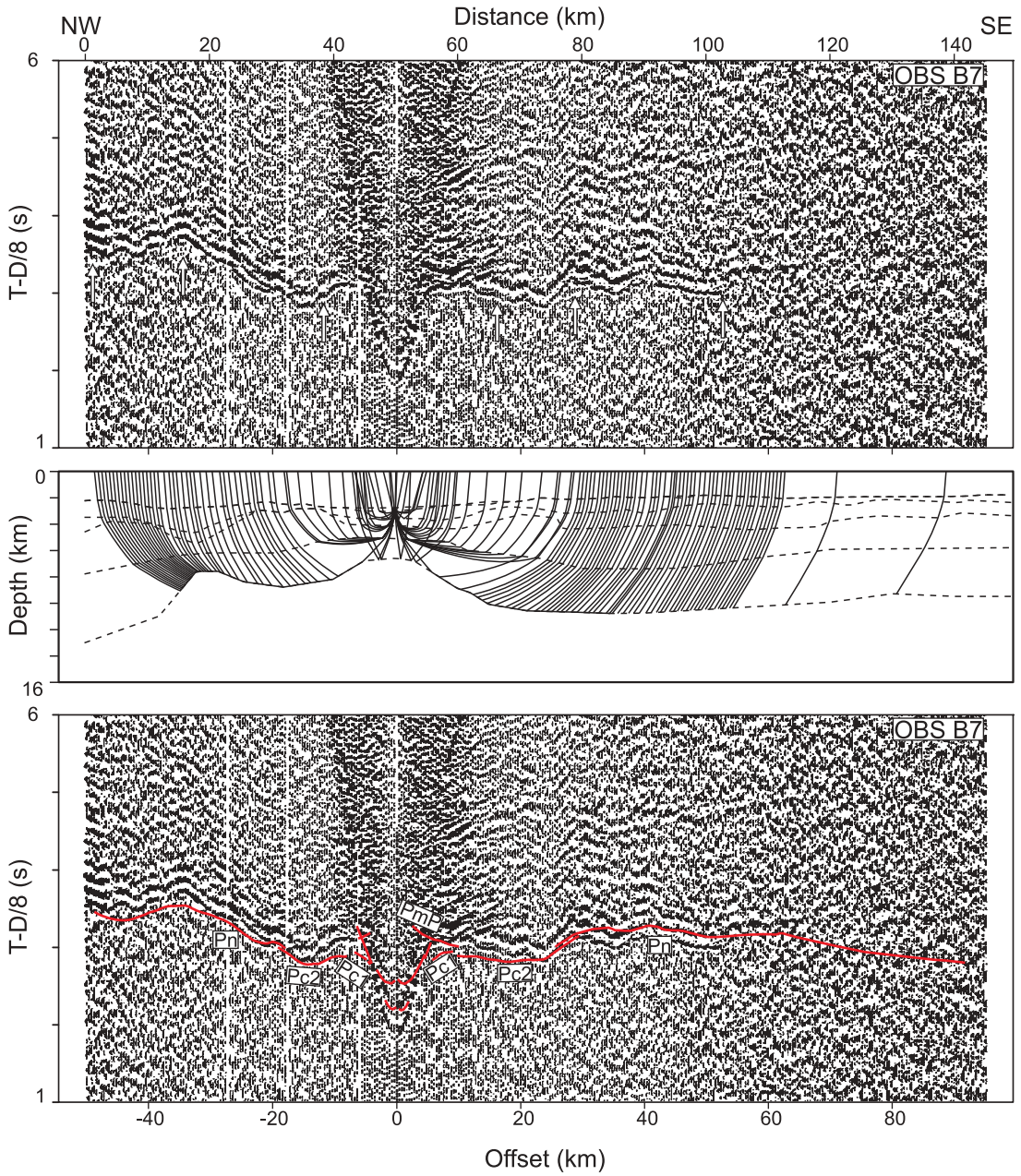

Figure 9. (top) Trace normalized record section for the vertical geophone of OBS B7. The horizontal scale is distance (upper) along the velocity model (Figure 2c) and distance (lower) from the OBS. The travel times are displayed with a reduction velocity of 8 km/s. Arrows indicate first arrivals. (middle) Ray-path diagram. (bottom) Trace normalized record section. Computed travel times from the revised modeling superimposed. See text for description of phases.

follow the depth of the basement. No distinct change is observed in the anomaly pattern from EGR Segment A to Segment B. The magnetic anomaly pattern along the crossing Line 1 (Figure 11a) shows increasing, positive anomalies over the Greenland Basin towards the GFZ. This culminates in a broad magnetic anomaly with a magnetic peak (~180 nT) over the GFZ approximately 10 km to the southwest of the EGR Segment B crest (Figure 11a, 80 km). Importantly, the magnitude of the anomaly decreases abruptly to −30 nT over the ridge crest itself and stays low over Segment A and the adjacent deep basins to the north. These observations point to an overall non-magnetic behavior of both Segments A and B. We therefore suggest that the positive magnetic anomaly reflects volcanics related to extension normal to the GFZ. This may explain the observed flexural uplift of Segments A and B along the GFZ (Figure 5) [cf. *Weissel et al.*, 1992; *Clift and Lorenzo*, 1999; *Bonatti et al.*, 2005]. Also the Line 1 MCS profile shows evidence of possible intrasedimentary sills within the half-graben to the southwest of the EGR (Figure 6a (bottom), 65–80 km). This interpretation is supported by a simple magnetic modeling Figure 12, showing that the observed magnetic anomaly at the GFZ may

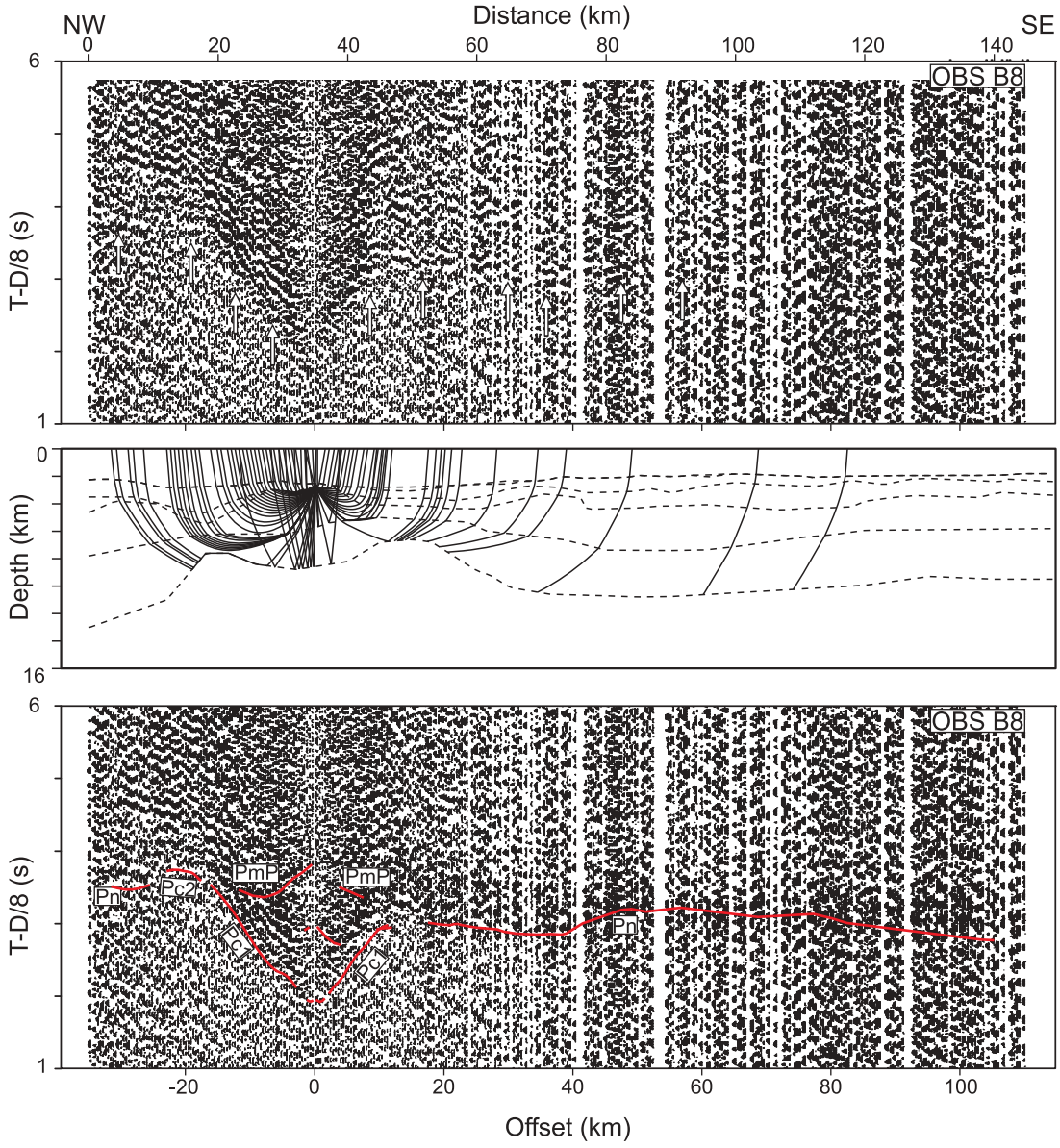

Figure 10. (top) Trace normalized record section for the vertical geophone of OBS B8. The horizontal scale is distance (upper) along the velocity model (Figure 2c) and distance (lower) from the OBS. The travel times are displayed with a reduction velocity of 8 km/s. Arrows indicate first arrivals. OBS B8 was affected by increased noise levels with a dominant frequency of 6.75 Hz, which was exactly within the seismic energy waveband (5–8 Hz) [*Døssing et al.*, 2008]. We experimented with various combinations of deconvolution, notch filtering and trace mix. Also, dip-filtering was considered. However, given the strong basement topography and thin crust, this was not successful. (middle) Ray-path diagram. (bottom) Trace normalized record section. Computed travel times from the revised modeling superimposed. See text for description of phases.

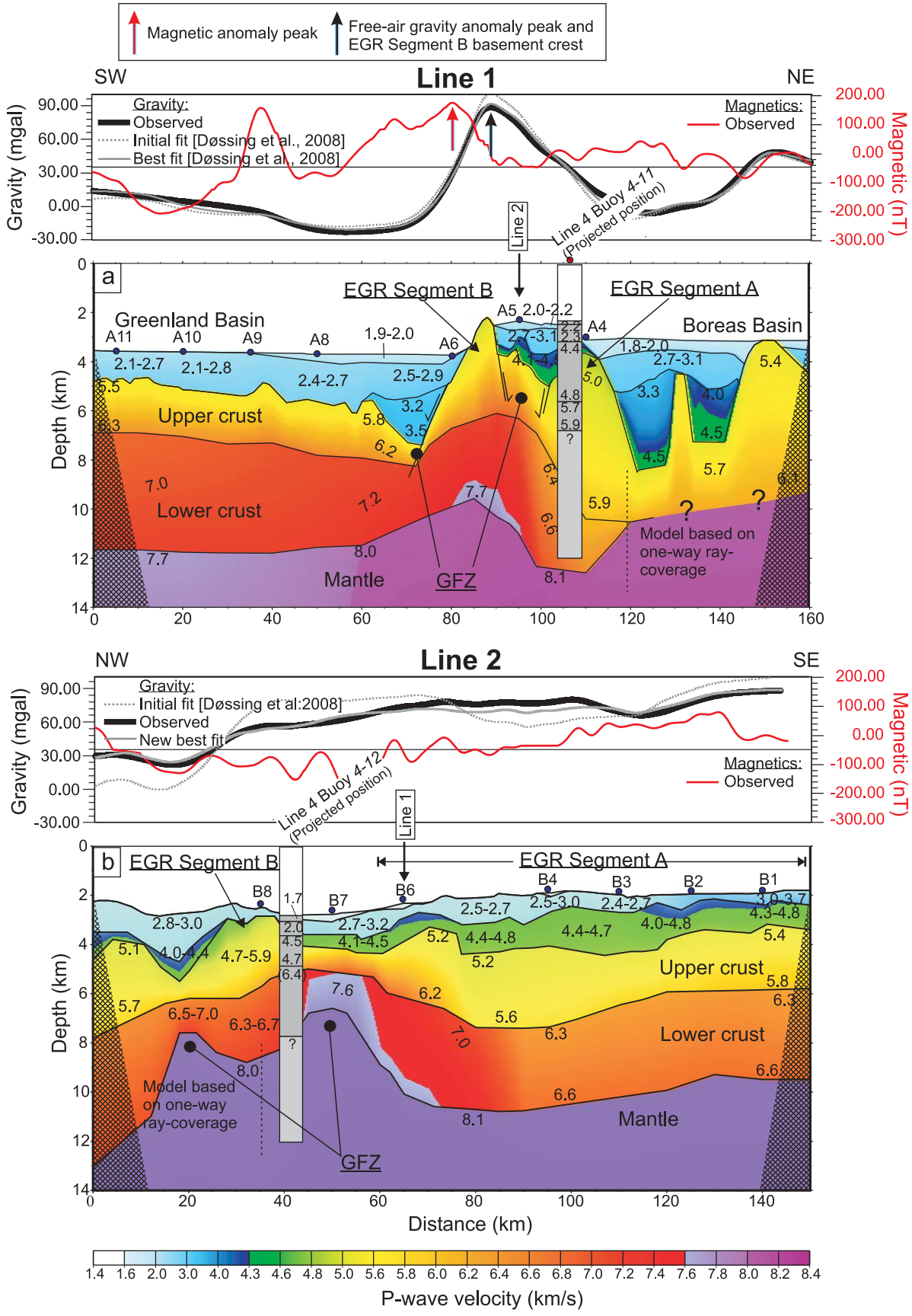
Magnetic anomaly peak
Free-air gravity anomaly peak and EGR Segment B basement crest
SW
Line 1
NE
Gravity (mgal)
Gravity:
Observed
Initial fit [Døssing et al., 2008]
Best fit [Døssing et al., 2008]
Magnetics:
Observed
Magnetic (nT)
Line 2
Line 4 Buoy 4-11 (Projected position)
a
EGR Segment B
EGR Segment A
Greenland Basin
Boreas Basin
Upper crust
Lower crust
Mantle
GFZ
Model based on one-way ray-coverage
Depth (km)
NW
Line 2
SE
Initial fit [Døssing et al:2008]
New best fit
Line 4 Buoy 4-12 (Projected position)
Line 1
b
Distance (km)
P-wave velocity (km/s)

Figure 11

Table 3. Phase Index, Type, Number of Observations (n), Picking Error (t_{est} (ms)), RMS Misfit Between Calculated and Picked Travel Times (t_{rms} (ms)), and Normalized X^2 for Important Phases of the Line 2 Revised Velocity Model[a]

Phase Index	Type	n	t_{est} (ms)	t_{rms} (ms)	X^2
		All OBSs			
P_{c2}	Refracted wave, lower crust	401	60–100	62(66)	0.68(0.70)
P_mP	Reflected wave, Moho	464	60–100	65(62)	0.92(0.80)
P_n	Refracted wave, upper mantle	999	100	132(163)	1.75(2.66)
		OBSs B7 and B8 Only			
P_{c2}	Refracted wave, lower crust	77	60–100	7(8.5)	0.53(0.71)
P_mP	Reflected wave, Moho	35	60–100	9(11)	0.77(0.94)
P_n	Refracted wave, upper mantle	337	100	17(22)	2.92(4.93)

[a]The numbers in parentheses refer to original values [*Døssing et al.*, 2008].

be explained by negatively magnetized oceanic crust (constant intensity of 5 A/m) in the adjacent Greenland Basin overlain by positively magnetized rocks within the half-graben and along the GFZ-fault-plane. In contrast, a model which includes magnetic source rocks at EGR Segment B, produces a significant misfit. Thus, the narrow magnetic peak (150 nT) which is located further out in the Greenland Basin (Figure 11a, 40 km) in oceanic crust of ~C23 age (early Eocene) may represent another indication of anomalous volcanic activity. This anomaly is located approximately above a basement mound which from MCS data appears to have intruded into the overlying sediments (Figure 6a (bottom), 40 km). We therefore interpret this mound as a buried volcano similar to basement mounds interpreted elsewhere in the Greenland Basin (T. Nielsen, GEUS, personal communication, 2010). Considering the intra-sedimentary setting of the volcanics in the GFZ-half-graben, the likely C23–C24A age of the underlying oceanic crust (see Figure 4a) and the ~C23 age for the Greenland Basin volcano, we estimate a minimum early Eocene (C23, 50.9 Ma) age for the volcanic activity.

[27] It is possible that the magnetic characteristics of Segment B are the result of oceanic crustal generation during a period without reversals. In this case, the crust should have formed over a relatively short period (1–1.5 mill. years) considering the frequency of magnetic reversals during the earliest Eocene – earliest Oligocene period [*Cande and Kent*, 1995]. However, it is difficult to explain how oceanic crust at Segment B would end up in en echelon pattern with the continental Segment A, and how to juxtapose possible oceanic crust at Segment B with the very deep (and possibly old) sedimentary basin located to the north of this and the EGR Central Segment (Figures 6a and 6b).

[28] Comparison of gravity profiles across the GFZ – EGR shows that a narrow, 20 mgal isostatic gravity anomaly coincides with the GFZ along EGR Segment B (Figure 13a). The anomaly is centered near the foot of the southwest flank of the ridge segment. A similar anomaly of 40 mgal is observed at the foot of the EGR Central Segment (Figure 13b), while almost no isostatic anomaly is observed along Segment A (Figure 13c). Wide-angle seismic and gravity modeling along Line 1 [*Døssing et al.*, 2008] indicate that the anomaly reflects increased lower crustal P wave velocities (7.1–7.7 km/s) and high densities (≥3000 kg/m^3) on either side of the GFZ. Importantly, the peak isostatic anomaly coincides with the peak of the modeled magnetic anomaly (Figure 13b), suggesting that the inferred volcanic intrusions and/or anomalous lower crust (i.e., a buried load [e.g., *Lin and Watts*, 2002]) near the GFZ at the EGR Central Segment (Figure 12) may continue to the northwest along the SW-flank of Segment B.

5.2. Two EGR Segments: Results of Plate Motion Changes?

[29] Spreading ridge-transform-ridge systems are very sensitive to small changes in spreading direction resulting from reorientations in the lithospheric stress field. Such changes are recorded by seafloor geophysical data [e.g., *Tucholke and Schouten*, 1989; *McCarthy et al.*, 1996; *Cande et al.*, 1995]. Transform migration and oscillatory spreading related to changes in relative plate motion has thus been proposed as explanation for anomalously old crust near oceanic transforms [*Bonatti and Crane*, 1982]. *Bonatti and Crane* [1982] present a model for the Vema Transform Zone (Central Atlantic), which infers that a minor change in spreading direction and axial ridge propagation produced a new ridge-transform-ridge geometry. This geometry is oriented at a minor angle to the old ridge-transform-ridge geometry. Similarly, the existence of a major aseismic valley at the Romanche transform (Central Atlantic) has been interpreted as the PaleoRomanche transform related to migration and reorientation of the transform [*Bonatti et al.*, 1994].

[30] In the earliest Oligocene (C13, 33.3 Ma), rotation in the lithospheric stress field between Greenland and Eurasia from a NW- to a WNW-direction forced migration of the GFZ transform and a northward axial rift propagation of the Mohns Ridge segment. This caused spreading to concentrate along proto-Knipovich Ridge segments to the N/NE of the EGR [*Mosar et al.*, 2002; *Faleide et al.*, 2008]. Hence,

Figure 11. Velocity models and interpretations along (a) Line 1 and (b) Line 2 (Revised model). Top images show ship-borne free-air gravity and magnetic anomaly data. Interpretations of EGR Segments A and B are based on results from this study. Note the difference in Line 2 interpretation compared with the original interpretation by *Døssing et al.* [2008] (Figure 2c). Also shown are one-dimensional velocity models for the nearby sonobuoys 4–11 and 4–12 from Line 4, which intersects Lines 1 and 2. Note that buoy 4–12 has been projected towards OBS B8 because this buoy mainly samples crustal velocities from beneath EGR Segment B rather than the fault zone between Segments A and B (i.e., OBS B7). See text for discussion.

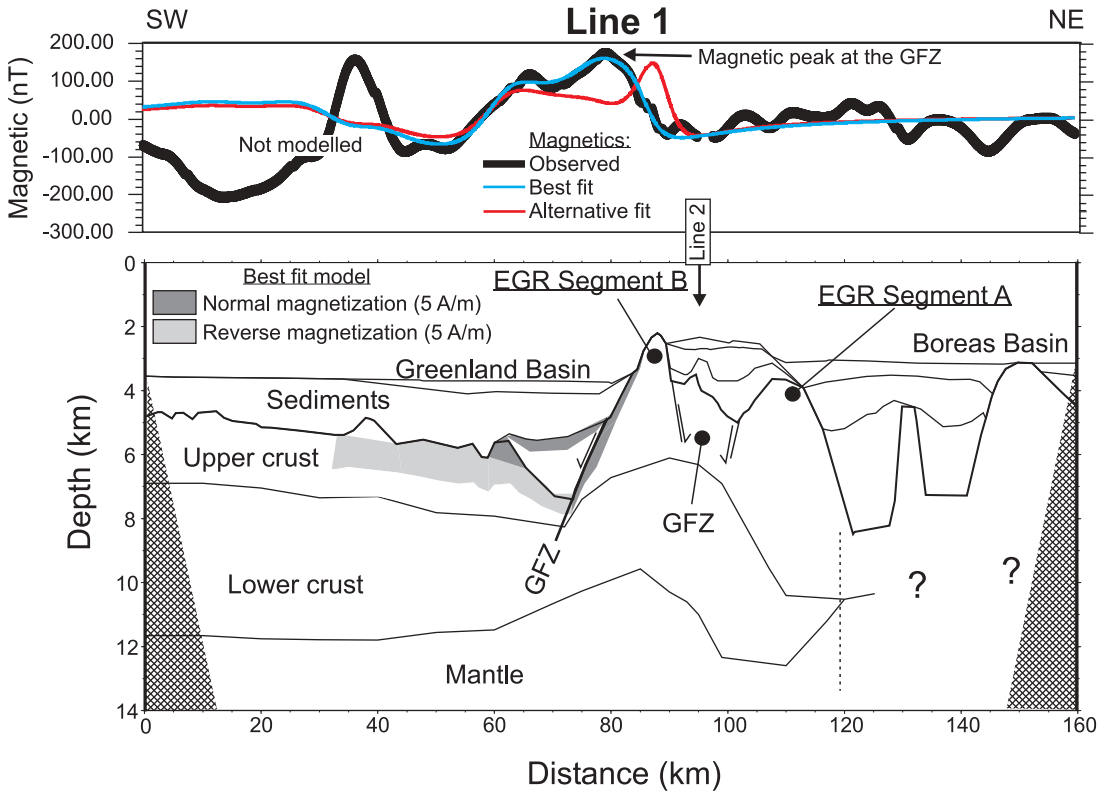

Figure 12. Magnetic modeling along Line 1. Blue line: Preferred model assuming a negatively magnetized oceanic crust (constant intensity of 5 A/m) in the Greenland Basin, overlain by positively magnetized rocks within the half-graben and along the GFZ-fault-plane. Red line: Alternative model assuming an additional 1-km-thick positive magnetic layer over EGR Segment B (intensity 1 A/m). Note the displacement between the modeled and observed peak of the positive magnetic anomaly near the GFZ. Note also that it was not attempted to model the magnetic anomaly over the proposed volcanic mound in the Greenland Basin due to the unfavorable orientation of the seismic profile, being (sub)parallel to the magnetic chrons (see Figure 4a.)

the EGR, formerly part of the SW Barents Sea margin (Eurasia plate), changed its sense of motion as it was transferred to the Greenland plate [*Engen*, 2005; *Faleide et al.*, 2008; *Døssing et al.*, 2008].

[31] Interpretation of the two transform ridges at the GFZ, the EGR Segments A and B, and their ~10° difference in orientation (Figure 4a) suggests another change in relative plate motion but prior to the known C13 changes. Such a change may have forced transform migration and reorientation of the early GFZ from initially to the south of Segment B to a position between Segments A and B, transferring Segment B from the Eurasia to the Greenland plate. The SE-termination of Segment B and the 10° change in orientation of the GFZ are located opposite oceanic crust of ~C22 age (early Eocene, 49.4 Ma) in the Greenland Basin (Figure 4a), which points to a possible change in relative plate motion at this time. This interpretation is consistent with the sharp C22-change in plate motion interpreted between Greenland and North America from a kink in magnetic flow lines in ocean basins in the Labrador Sea and to the south of Iceland [*Gaina et al.*, 2009] and in the Norway Basin [*Gernigon et al.*, 2011]. A similar, sharp kink has not been interpreted in the Greenland Basin, which has been suggested to relate to internal deformation of the Greenland plate or complex re-adjustment of the NE Atlantic plate boundary, taking up the C22-changes [*Gaina et al.*, 2009]. However, the new data and interpretations presented in this study suggest that minor plate motion changes did take place at the GFZ around this time, possible relating to the changes further south. This interpretation is shown in a simplified structural-kinematic model of the GFZ – EGR in Figure 14. Alternatively, the formation of the two, non-parallel EGR segments may relate to pre-inherited, continental basement structures.

6. Conclusions

[32] We present a revised interpretation of the GFZ - EGR by integrating a range of existing and new geophysical data, including quality-controlled vintage ship soundings, existing seismic reflection and refraction data, the latest global satellite gravity model as well as new multi-beam data, MCS reflection data, sonobuoy seismic data and ship-track magnetic anomaly data. We also compile a new 2.5 × 2.5 km bathymetric grid for the area. Combined interpretation of the data sets show the following:

[33] 1. The EGR is composed of two overstepping ridge segments (EGR Segments A and B) of which Segment A corresponds to the previously interpreted continental EGR

[*Døssing et al.*, 2008] while Segment B has not been detected before.

[34] 2. EGR Segment B is likely composed of thinned, non-magnetic continental crust similar to the crust beneath Segment A.

[35] 3. Positive magnetic anomalies along the GFZ may be modeled by intra-sedimentary magnetic source rocks immediately to the southwest of the EGR and along the GFZ-fault-plane, thus indicating volcanic activity associated with the fracture zone. We estimate a minimum early Eocene (C23) age for the volcanic activity.

[36] 4. The EGR Segments are bounded by portions of the GFZ with a distinct 10–15° difference in orientation. This is suggested to relate to a minor change in the regional stress pattern around anomaly C22 time (early Eocene), which forced a transform migration and reorientation of the GFZ from initially to the south of Segment B to a position between Segments A and B.

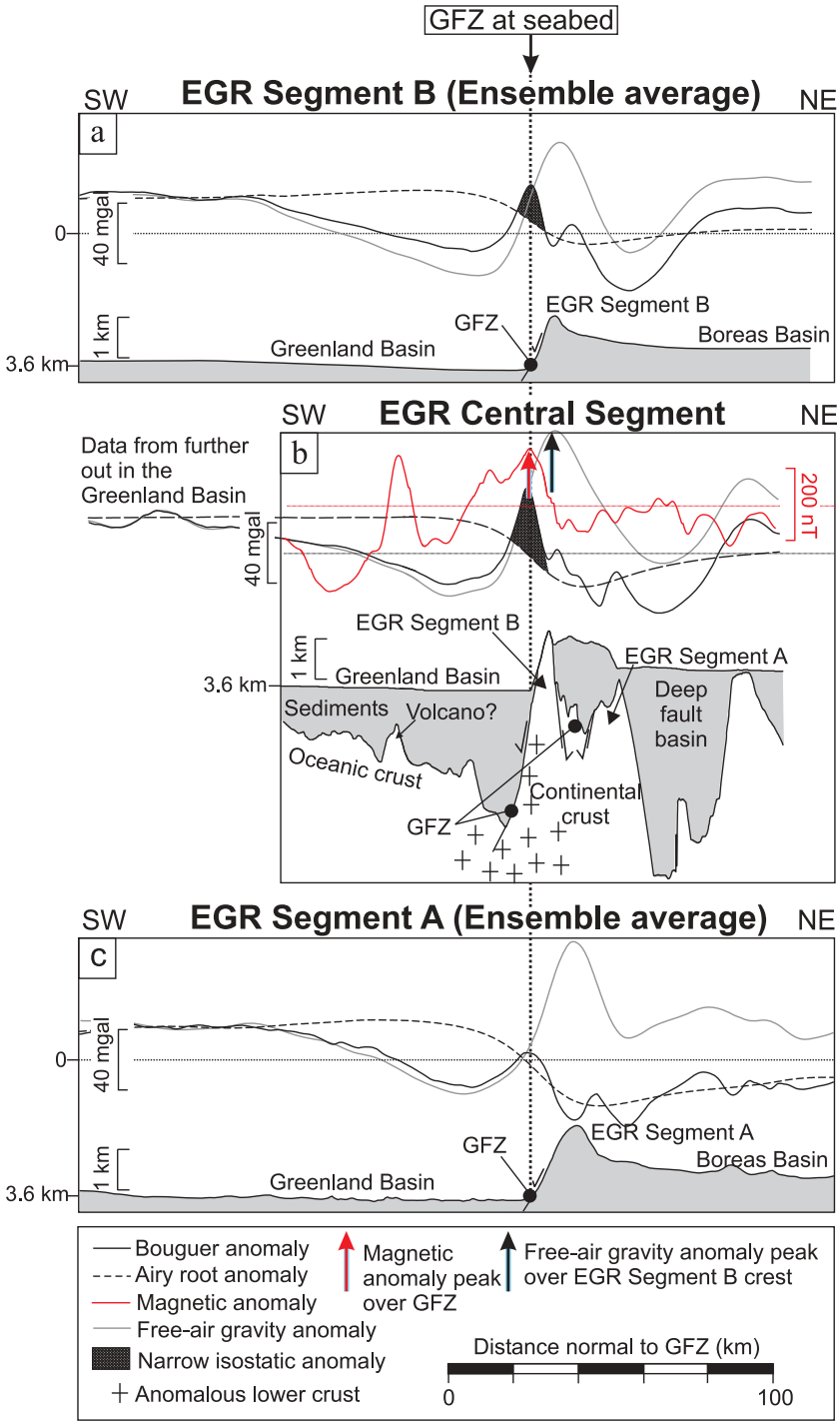

Figure 13

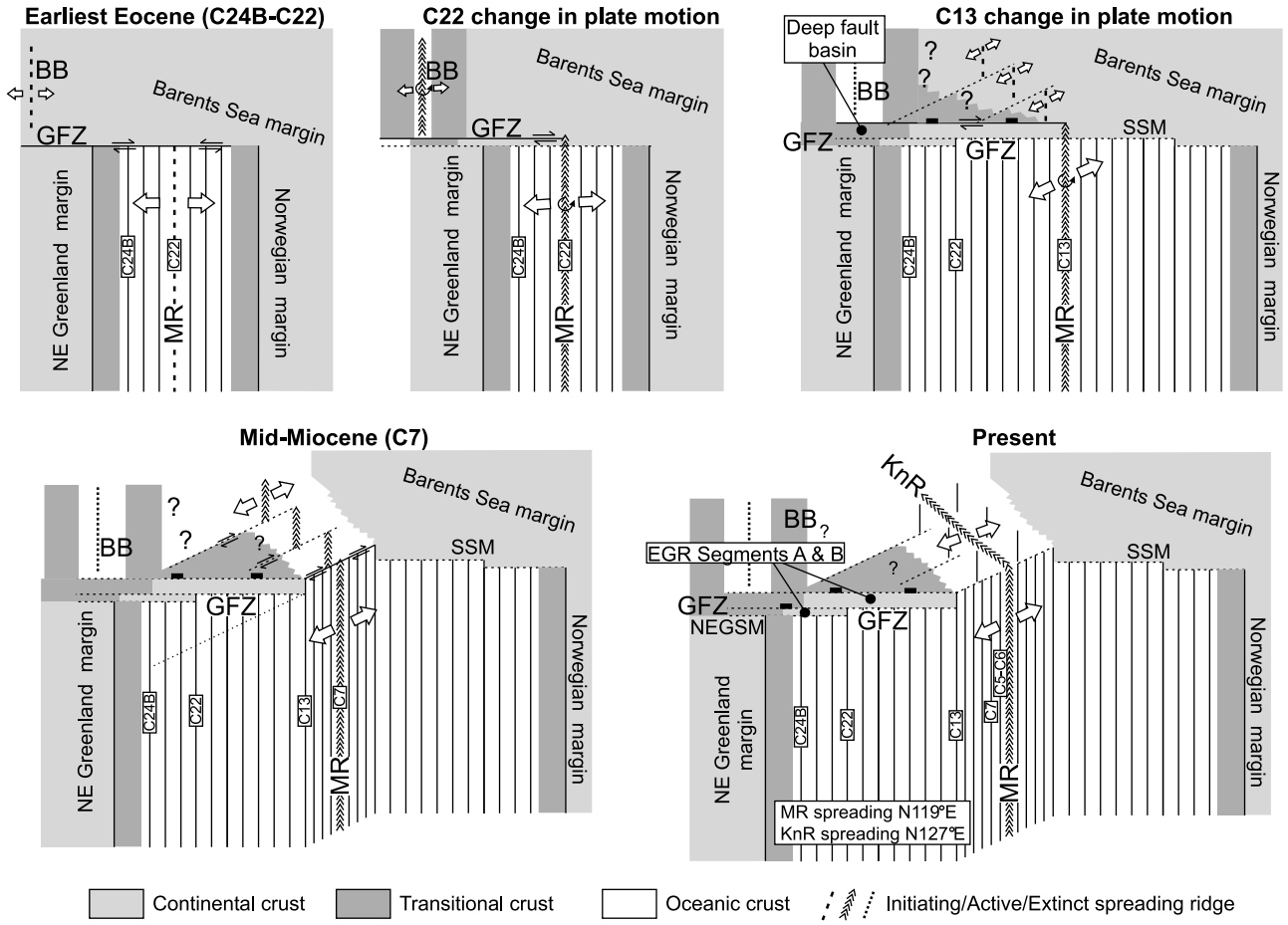

Figure 14. Simplified Cenozoic structural-kinematic evolution of the GFZ–EGR with the proposed C22- and C13-changes in relative plate motion. Note that the proposed direction of rotation of the C22 stress field is tentative. BB, Boreas Basin; EGR, East Greenland Ridge; GFZ, Greenland Fracture Zone; NEGSM, NE Greenland Shear Margin; SSM, Senja Shear Margin.

Figure 13. Comparison of ship-track profiles of bathymetry, satellite free-air, Bouguer and Airy root gravity anomalies across: (a) EGR Segment B, (b) the EGR Central Segment (basement geometry adopted from Figure 11a) and (c) EGR Segment A. Note that magnetic ship-track anomalies are also shown across the EGR Central Segment. The profiles in Figures 13a and 13c were produced by spectral ensemble averaging of profiles that cross the GFZ at these EGR segments (see Figure 5), while the profile across the Central Segment is simply Line 1 (see Figure 11a). Ensemble averaging is a spectral technique that retains features that are common to all profiles and generally suppresses features that are present on only a few profiles [*Watts et al.*,2000], i.e., the profiles in Figures 13a and 13c show the common bathymetric and gravity features across Segments A and B, respectively. All profiles were projected onto lines normal to the GFZ prior to ensemble averaging. The Bouguer and Airy root anomalies were calculated using a crustal density of 2670 kg/m^3 and a density contrast at Moho of 330 kg/m^3. The Airy isostatic anomaly was calculated by subtracting the gravity effect of the Airy root from the Bouguer anomaly. Note that because the seabed in the Greenland Basin is characterized by a broad positive gravity anomaly [*Døssing et al.*, 2008], which likely reflects sources at or below the crust, we have added 35 mgal to the Airy root anomaly prior to subtracting it [cf. *Lin and Watts*, 2002]. By comparing the Bouguer anomaly with the gravity effect of the Airy Moho, the Bouguer anomaly is divided into a negative part in the Greenland Basin that may be the result of flexure and a short wavelength positive isostatic anomaly over the GFZ and SW-flank of the EGR (mainly in Figures 13a and 13c) that may be attributed to a buried load [cf., *Lin and Watts*, 2002]. Additional tests showed that overall similar isostatic results are obtained when using a lower crustal density of 2200 kg/m^3 instead of 2670 kg/m^3 in the calculation of Bouguer anomalies and the Airy root anomaly, i.e., isostatic anomalies are observed over Segment B and the Central Segment but not over Segment A. We prefer, however, to use 2670 kg/m^3 as representative density, because of the crystalline crustal density of the EGR ridge crests at–or close to–the sea bed.

[37] **Acknowledgments.** Thanks to the Alfred Wegener Institute (AWI) and the Geological Survey of Denmark and Greenland (GEUS) for providing access to seismic data. Thanks to W. Stratford (Univ. of Durham, UK), T. Dahl-Jensen (GEUS) and A. B. Watts (Univ. of Oxford, UK) for helpful comments. Thanks also to Tim Minshull and one anonymous reviewer for very constructive comments. One of the authors (AD) was formerly supported by a doctoral fellowship from the Faculty of Science, Univ. of Copenhagen. The seismic data along Lines 1 (GEUS2002-1), 2 (GEUS2002-2) and 4 (LOMROG-4) and the multi-beam bathymetric data were collected as part of the Danish Continental Shelf Project. Funding for this project were provided by the Danish Ministry of Science, Technology and Innovation. We thank Martin Jakobsson and Morten Sølvsten for the processing of the multi-beam data and for making them available to us. Thanks also to John R. Hopper (GEUS) processing the multi-channel seismic Line 4. The paper is published with permission from the Geological Survey of Denmark and Greenland (GEUS).

References

Andersen, O. B., P. Knudsen, P. Berry, J. Freeman, N. Pavlis, and S. Kenyon (2008), The DNSC07a ocean-wide altimetry-derived gravity anomaly field, paper presented at European Geosciences Union General Assembly, Vienna, 18 April.

Anderson, L., G. Björk, P. Eriksson, S. Hjalmarsson, S. Jutterstöm, A. Olsson, J. Nilsson, and F. Zemlyak (2007), Lomonosov Ridge off Greenland (LOMROG) 2007: Chemical and Physical Oceanography, in *Swedish Polar Research Secretariat Yearbook 2007*, pp. 127–129, Swed. Polar Res. Secr., Stockholm.

Berger, D., and W. Jokat (2008), A seismic study along the east Greenland margin from 72°N to 77°N, *Geophys. J. Int.*, *174*, 733–748, doi:10.1111/j.1365–246x.2008.03794.x.

Berger, D., and W. Jokat (2009), Sediment deposition in the northern basins of the North Atlantic and characteristic variations in shelf sedimentation along the east Greenland margin, *Mar. Petr. Geol.*, *26*, 1321–1337, doi:10.1016/j.marpetgeo.2009.04.005.

Bonatti, E., and K. Crane (1982), Oscillatory spreading explanation of anomalously old uplifted crust near oceanic transforms, *Nature*, *300*, 343–345.

Bonatti, E., M. Ligi, L. Gasperini, A. Peyve, Y. Raznitsin, and Y. Chen (1994), Transform migration and vertical tectonics at the Romanche fracture zone, equatorial Atlantic, *J. Geophys. Res.*, *99*, 21,779–21,802, doi:10.1029/94JB01178.

Bonatti, E., D. Brunellia, W. R. Buck, A. Cipriania, P. Fabrettia, V. Ferrantea, L. Gasperinia, and M. Ligia (2005), Flexural uplift of a lithospheric slab near the Vema transform (central Atlantic): Timing and mechanisms, *Earth Planet. Sci. Lett.*, *240*, 642–655, doi:10.1016/j.epsl.2005.10.010.

Bruguier, N. J., and T. A. Minshull (1997), Accurate modelling of sonobuoy refraction data to determine velocity variations in oceanic crust, *Mar. Geophys. Res.*, *19*, 25–36.

Cande, S., and D. Kent (1995), Revised calibration of the geomagnetic polarity timescale for the late cretaceous and cenozoic, *J. Geophys. Res.*, *100*, 6093–6095.

Cande, S., C. Raymond, J. Stock, and W. Haxby (1995), Geophysics of the Pitman fracture zone and Pacific-Antarctic plate motions during the Cenozoic, *Science*, *270*, 947–953, doi:10.1126/science.270.5238.947.

Clift, P. D., and J. M. Lorenzo (1999), Flexural unloading and uplift along the Côte d'Ivoire-Ghana Transform Margin, equatorial Atlantic, *J. Geophys. Res.*, *104*, 25,257–25,274.

Doré, A. G., E. R. Lundin, N. J. Kusznir, and C. Pascal (2008), Potential mechanisms for the genesis of Cenozoic domal structures on the NE Atlantic margin: Pros, cons and some new ideas, *Geol. Soc. Spec. Publ.*, *306*, 1–26, doi:10.1144/SP306.1.

Døssing, A., T. Dahl-Jensen, H. Thybo, R. Mjelde, and Y. Nishimura (2008), East Greenland Ridge in the North Atlantic Ocean: An integrated geophysical study of a continental sliver in a boundary transform fault setting, *J. Geophys. Res.*, *113*, B10107, doi:10.1029/2007JB005536.

Døssing, A., L. Stemmerik, T. Dahl-Jensen, and V. Schlindwein (2010), Segmentation of the eastern north Greenland oblique-shear margin — Regional plate tectonic implications, *Earth Planet. Sci. Lett.*, *292*(3–4), 239–253, doi:10.1016/j.epsl.2009.12.036.

Eldholm, O., J. I. Faleide, and A. M. Myhre (1987), Continent ocean transition at the western Barents Sea/Svalbard continental margin, *Geology*, *15*(12), 1118–1122.

Engen, Ø. (2005), Evolution of high Arctic ocean basins and continental margins, Ph.D. thesis, 184 pp., Univ. of Oslo, Norway.

Engen, Ø., J. I. Faleide, and T. K. Dyreng (2008), Opening of the Fram Strait gateway: A review of plate tectonic constraints, *Tectonophysics*, *450*, 51–69, doi:10.1016/j.tecto.2008.01.002.

Faleide, J. I., E. Vaagnes, and S. T. Gudlaugsson (1993), Late Mesozoic–Cenozoic evolution of the south-western Barents Sea in a regional rift-shear setting, *Mar. Petr. Geol.*, *10*, 186–214.

Faleide, J. I., F. Tsikalas, A. J. Breivik, R. Mjelde, O. Ritzmann, Ø. Engen, J. Wilson, and O. Eldholm (2008), Structure and evolution of the continental margin off Norway and the Barents Sea, *Episodes*, *31*, 82–91.

Gaina, C., L. Gernigon, and P. Ball (2009), Paleocene—Recent plate boundaries in the NE Atlanic and the formation of the Jan Mayen microcontinent, *J. Geol. Soc.*, *166*, 606–616.

Gernigon, L., et al. (2011), The Norway Basin revisited from break-up to ridge abortion, *Mar. Pet. Geol.*, in press.

Haakansson, E., and S. A. S. Pedersen (1982), Late Paleozoic to Tertiary tectonic evolution of the continental margin in north Greenland, in *Arctic Geology and Geophysics*, edited by A. Embry and H. Balkwill, *Mem. Can. Soc. Pet. Geol.*, 8, 331–348.

Haakansson, E., and S. A. S. Pedersen (2001), The Wandel Hav Strike-Slip Mobile Belt – A Mesozoic plate boundary in north Greenland, *Bull. Geol. Soc. Den.*, *48*(2), 149–158.

Haakansson, E., and L. Stemmerik (1989), Wandel Sea Basin – A new synthesis of the late Paleozoic to Tertiary accumulation in north Greenland, *Geology*, *17*, 683–686.

Hamann, N. E., R. C. Whittaker, and L. Stemmerik (2005), Geological development of the northeast Greenland shelf, in *Petroleum Geology: North-West Europe and Global Perspectives: Proceedings of the 6th Petroleum Geology Conference*, edited by A. G. Dore and B. A. Vining, pp. 887–902, Geol. Soc., London.

Harland, W. B. (1969), Contribution of Spitsbergen to understanding of tectonic evolution of the North Atlantic region, in *Geology and Continental Drift*, vol. 12, edited by M. Kay, pp. 817—851, Am. Assoc. of Pet. Geol., Tulsa, Okla.

Jakobsson, M., N. Z. Cherkis, J. Woodward, R. Macnab, and B. Coakley (2000), New grid of Arctic bathymetry aids scientists and mapmakers, *Eos Trans. AGU*, *81*(9), 89.

Jakobsson, M., C. Marcussen, and LOMROG Scientific Party (2008a), *Lomonosov Ridge Off Greenland 2007 (LOMROG): Cruise Report*, 122 pp., Geol. Surv. Den. and Greenl., Copenhagen.

Jakobsson, M., R. Macnab, M. Mayer, R. Anderson, M. Edwards, J. Hatzky, H. W. Schenke, and P. Johnson (2008b), An improved bathymetric portrayal of the Arctic Ocean: Implications for ocean modeling and geological, geophysical and oceanographic analyses, *Geophys. Res. Lett.*, *35*, L07602, doi:10.1029/2008GL033520.

Kalsbeek, F., and H. Jepsen (1983), The Midsommersø Dolerites and associated intrusions in the Proterozoic platform of eastern north Greenland—A study of the interaction between intrusive basic magma and sialic crust, *J. Petrol.*, *24*, 605–634.

Lin, A. T., and A. B. Watts (2002), Origin of the West Taiwan basin by orogenic loading and flexure of a rifted continental margin, *J. Geophys. Res.*, *107*(B9), 2185, doi:10.1029/2001JB000669.

Ludwig, W. J., J. E. Nafe, and C. L. Drake (1970), Seismic refraction, in *The Sea, New Concepts of Sea Floor Evolution: Part I, General Observations*, vol. 4, edited by A. E. Maxwell, pp. 53—84, Wiley-Interscience, Hoboken, N. J.

McCarthy, M. C., S. Kruse, M. Brudzinski, and M. Ranieri (1996), Changes in plate motions and the shape of Pacific fracture zones, *J. Geophys. Res.*, *101*, 13,715–13,730.

McClay, K. R., M. G. Norton, P. Coney, and G. H. Davis (1986), Collapse of the Caledonian orogen and the Old Red Sandstone, *Nature*, *323*, 147–149.

Mosar, J., and J. G. Opsal (2002), Plate tectonic model for the separation of Greenland and Svalbard and the formation of the Boreas Basin, in *Onshore-Offshore Relationships on the Nordic Atlantic Margin*, vol. 2, edited by A. Hurst, pp. 137–139, NGF Abstr. and Proc., Trondheim, Norway.

Mosar, J., T. Torsvik, and the BAT Team (2002), Opening of the Norwegian and Greenland seas: Plate tectonics in mid Norway since the Late Permian, in *BATLAS-Mid Norway Plate Reconstruction Atlas With Global and Atlantic Perspectives*, edited by E. A. Eide, pp. 48–59, Geol. Surv. of Norway, Trondheim, Norway.

Surlyk, F., L. B. Clemmensen, and H. C. Larsen (1981), Post-Paleozoic evolution of the east Greenland continental margin, in *Geology of the North Atlantic Borderlands*, edited by J. Kerr and A. Ferguson, *Mem. Can. Soc. Pet. Geol.*, 7, 611–645.

Talwani, M., and O. Eldholm (1977), Evolution of the Norwegian-Greenland Sea, *Geol. Soc. Am. Bull.*, *88*, 969–999.

Tucholke, B. E., and H. Schouten (1989), Kane fracture zone, *Mar. Geophys. Res.*, *10*, 1–3, doi:10.1007/BF02424659.

Watts, A. B., W. S. Mckerrow, and E. Fielding (2000), Lithospheric flexure, uplift, and landscape evolution in south-central England, *J. Geol. Soc. Lond.*, *157*, 1169–1177.

Weissel, J. K., V. A. Childers, and G. D. Karner (1992), Extensional and compressional deformation of the lithosphere in the light of ODP drilling in the Indian Ocean, in *The Indian Ocean: A Synthesis of Results From the Ocean Drilling Program*, *Geophys. Monogr. Ser.*, vol. 70, edited by R. A. Duncan et al., pp. 413–664, AGU, Washington, D. C.

White, R. S., D. P. McKenzie, and R. K. O'Nions (1992), Oceanic crustal thickness from seismic measurements and rare Earth element inversions, *J. Geophys. Res.*, *97*, 19,683–19,715.

Zelt, C. A., and D. A. Forsyth (1994), Modeling wide-angle seismic data for crustal structure: Southeastern Grenville Province, *J. Geophys. Res.*, *99*, 11,687—11,704.

Zelt, C. A., and R. B. Smith (1992), Seismic traveltime inversion for 2-D crustal velocity structure, *Geophys. J. Int.*, *108*, 16–34, doi:10.1111/j.1365–246X.1992.tb00836.x.

Zinck-Jørgensen, K. (1994), The Trolle Land Fault System, Kim Fjelde, eastern Peary Land, in *Wandel Sea Basin: Basin Analysis*, edited by E. Haakansson, pp. 1–17, Univ. of Copenhagen, Copenhagen.

A. Døssing, National Space Institute, DTU Space, Juliane Maries Vej 30, DK-2100 Copenhagen, Denmark. (ards@space.dtu.dk)

T. Funck, Geological Survey of Denmark and Greenland, Øster Voldgade 10, DK-1350 Copenhagen, Denmark.